# X-ray Powder Diffraction in Education:

## Part I, Bragg peak profiles

R. E. Dinnebier[1], P. Scardi[2]

[1] Max Plank Institute for Solid State Research, Heisenbergstrasse 1, 70569 Stuttgart, Germany

[2] Department of Civil, Environmental & Mechanical Engineering, University of Trento, via Mesiano 77, 38123 Trento, Italy

## Synopsis

Peak profile functions in powder diffraction are presented with the support of Mathematica® scripts, easily usable by interested readers, to explore the effect of different instrumental and microstructural parameters. Subsequent articles will illustrate the most common aberrations to the measured patterns and then total scattering methods.

## Abstract

A collection of scholarly scripts dealing with the mathematics and physics of peak profile functions in X-ray powder diffraction has been written using the Wolfram language in Mathematica®[1]. Common distribution functions, the concept of convolution in real and Fourier space, instrumental aberrations, and microstructural effects are visualized in an interactive manner and explained in detail. This paper is the first part of a series dealing with the mathematical description of powder diffraction patterns for teaching and education purposes.

## Introduction

X-ray powder diffraction (XRPD), an established technique for the study of crystal structures, finds increasing application toward qualitative and quantitative phase analysis and the study of microstructure for micro- and nanocrystalline materials.

For the study of crystalline materials, a powder pattern can be divided into Bragg reflections and background, where the latter among other contributions contains diffuse scattering from the sample. Bragg reflections are characterized by their position, intensity, breadth, and shape, each containing a wealth of information (Dinnebier & Billinge, 2008, Dinnebier, Leineweber & Evans, 2018).

[1] All scripts have been written in Wolfram Mathematica®, version 12.1.1.0 and are constantly updated. They are freely available at the TOPAS Wiki website http://topas.dur.ac.uk/topaswiki. Non-subscribers of Mathematica can run the scripts using the freely available Wolfram Player at https://www.wolfram.com/player/. Bugs and problems should be reported to r.dinnebier@fkf.mpg.de.

Computer programs for fitting peak profiles in powder diffraction perform either single peak fits or whole powder profile fitting (WPPF) with or without a structural model. Many programs have in common the ability to work like a black box for the user. It is frequently the case that some parameters are little affected by the non-linear least squares procedure, while others change wildly. In particular, among non-experts, a lot of confusion exists regarding the meaning and significance of fixed or refined parameters, their contribution to the Bragg peaks, the quality of the fit, the range of convergence, precision and accuracy, meaning and reliability of standard deviations, etc. In addition, many functions describing a physical effect show discontinuities, and the refined parameters are typically restricted by physical boundaries. Understanding the algorithms is necessary for a correct use of the software and assessment of the reliability of results.

In this series of papers dealing with the description and visualisation of mathematical functions used to describe a powder pattern, we present a collection of user-friendly, interactive, and freely distributable Mathematica® (Wolfram Research, 2020) teaching scripts. In particular, the so-called "Manipulate" option of Mathematica is extensively used to visualize the impact of parameters in an interactive manner. When possible, parameters from real life examples are default. The idea is "learn by doing", to gain intuition for what a mathematical model does to the diffraction peaks in a powder pattern and what are the limitations of said model, since every model is always an oversimplification of the underlying physics.

All parameters of the scripts are taken from the two well-established programs TOPAS (Coelho, 2018) and WPPM (Scardi & Leoni, 2001, 2002; Scardi *et al*. 2018, Scardi, 2020).

For the moment, the following three parts of this series are in preparation:

1. Part I, the peak profile of a powder pattern (this paper)
2. Part II, common correction functions in powder diffraction
3. Part III, total scattering

In this first paper, the various contributions to the peak profile in a powder diffraction pattern are described in terms of physical models and the effect they have on the peak shape. In general, the profile of a Bragg peak has contributions from the diffractometer and the microstructure of the sample. In the last few decades, a variety of sophisticated techniques and computer programs for analysing the peak shape of a powder pattern have been developed (Dinnebier & Billinge, 2008).

In general, the profile $\Phi(x')$ of a Bragg reflection centred at the peak position $X_0$ can be approximated by mathematical convolution (denoted by the symbol ∘) of contributions from the instrument, the so-called instrumental resolution function $IRF$, and from the microstructure $MS$ of the sample (Klug & Alexander, 1974):

$$\Phi(x') = (IRF \circ MS)(x') \qquad (1)$$

with

$$x' = X - X_0, \qquad (2)$$

where X is the observed peak position on the scale in which the data are recorded or analyzed. The profile function is therefore described relative to the peak centre $X_0$.

Since the majority of powder patterns are directly measured as a function of the scattering angle $2\theta$ in *degrees*, we will use $2\theta$ as independent variable for our profile functions throughout the text. It is worth noting here that many of the aberrations, to be discussed in Part II, are specifically $2\theta$-dependent. The conversion to reciprocal space in $nm^{-1}$ is given by the Bragg equation:

$$\lambda = 2\, d_{hkl} \sin\theta \;\Rightarrow d^* = \frac{1}{d_{hkl}} = \frac{2\sin\theta}{\lambda} \qquad (3)$$

with the wavelength $\lambda$ in *nm* and the distance between lattice planes $d_{hkl}$ with indices *hkl* in *nm*. Other scales besides $2\theta$, $d_{hkl}$ and $d^*$ include $Q$ (=$2\pi\, d^*$), TOF (time of flight), and E (energy). The conversion factor

$$c = \frac{\pi}{180}\frac{\cos\theta}{\lambda} \qquad (4)$$

which follows from the differential of the Bragg equation applies to change space from $2\theta$ in *degrees* to $d^*$ in $nm^{-1}$.[2] The Fourier-transformation (*FT*) of a function in $2\theta$-space in degrees leads to a function with reciprocal angle and units of $degree^{-1}$ that we will use for illustrative purpose only. The FT of a function in $d^*$- space and units of $nm^{-1}$ leads to a function in *nm* on a length scale in real space.

The instrumental resolution function itself can be considered a convolution of contributions coming from the finite width of the X-ray source (X-ray tube or synchrotron), the so-called emission profile, and a series of horizontal and vertical instrumental aberrations due to the diffractometer. In the most popular configuration, these include the angular acceptance function of the Soller slit(s) controlling the axial beam divergence, the angular acceptance function of the plug-in slit controlling the equatorial beam divergence, the angular acceptance function of the receiving slit, etc. For linear position sensitive detector (PSD) systems, the receiving slit aberration is replaced by functions describing the defocusing due to asymmetric diffraction, the parallax error and the point spread function of the detector.

$$IRF(x') = (Instr_1 \circ Instr_2 \circ Instr_3 \circ \ldots)(x') \qquad (5)$$

The same principle holds for the microstructure contribution of the sample, which can be viewed as a convolution of contributions from effects like size of coherently scattering domains, isotropic and/or anisotropic microstrain, faulting etc.

$$MS(x') = (Sam_1 \circ Sam_2 \circ Sam_3 \circ \ldots)(x') \qquad (6)$$

Equations 5 and 6 implicitly assume that all components of the convolution are independent which is a common approximation but not exact for microstructural parameters.

[2] The factor $\pi/180$ is used to convert an angular value given in degrees (e.g. the breadth of a reflection) to radians.

To describe the peak shape in a powder diffraction pattern, two approaches are common nowadays: (1) ideally, all contributions and their mathematical description are known. The resulting peak shape can thus be calculated from first principles. For building the *IRF*, the fundamental parameters (FP) approach (Cheary & Coelho, 1992, 1998) and for the *MS* the Whole Powder Pattern Modelling (WPPM) concept (Scardi & Leoni, 2001, 2002) are quite common. (2) Alternatively, owing to the fact that many contributions to powder diffraction peaks have a nearly Gaussian or Lorentzian shape, the Voigt-function, which is a convolution of Gaussian and Lorentzian components, or more commonly the pseudo-Voigt function for faster computation, is widely used to describe peak profiles in powder diffraction. It is important to note that the latter approach is empirical, and all interpretations of microstructural parameters based on the Voigt profile must be carefully evaluated.

As a matter of fact, real instruments are always more complex than any possible FP model. The differences between model and reality can be a source of systematic errors with the risk of ignoring some features of the IRF. As a commonly accepted compromise, the *IRF* is obtained by fitting a line profile standard with virtual no microstructural contributions using an empirical Voigt-profile, eventually convoluted with some instrumental aberration functions. In contrast, the MS is derived from more physical or at least phenomenological functions with few but meaningful parameters.

## Fourier transformation and convolution

The Fourier transformation (FT) greatly simplifies the convolution process and reveals many important properties of the peak profile, making it a good mathematical procedure to begin with.

The FT of a function $f(x)$ is a complex function defined as

$$F(s) = \sqrt{\frac{|b|}{(2\pi)^{1-a}}} \int_{-\infty}^{\infty} f(x)\, \mathrm{e}^{\mathrm{i}bsx}\, \mathrm{d}x$$
$$= \sqrt{\frac{|b|}{(2\pi)^{1-a}}} \int_{-\infty}^{\infty} f(x)\, (\cos(bsx) + \mathrm{i}\sin(bsx))\mathrm{d}x \qquad (7)$$

The Fourier integral transforms a function $f(x)$ ($x$ in real space) by an integral over cosine and sine functions to $F(s)$ ($s$ in reciprocal space = Fourier space). Some common choices for the Fourier parameters {a, b} which have a big impact on scaling are {0,1} (modern physics), {1,-1} (pure mathematics; systems engineering), {-1,1} (classical physics), {0,-2 $\pi$} (signal processing), {0,2 $\pi$} (crystallography).

The back transformation is given by:

$$f(x) = \sqrt{\frac{|b|}{(2\pi)^{1-a}}} \int_{-\infty}^{\infty} F(s)\, \mathrm{e}^{-bisx}\, \mathrm{d}x \qquad (8)$$

$$= \sqrt{\frac{|b|}{(2\pi)^{1-a}}} \int_{-\infty}^{\infty} F(s)(\cos(bsx) - \mathrm{i}\sin(bsx))\mathrm{d}s.$$

The independent variables, $s$ and $x$, are reciprocal to one another, so the exponent of the exponential function is dimensionless. If $x$ is in position space, $s$ is in "Fourier space" or "reciprocal space". In the following, we will use the crystallographic Fourier parameters {0,2 $\pi$} for simplicity:

$$F(s) = \int_{-\infty}^{\infty} f(x)\, \mathrm{e}^{2\pi \mathrm{i} s x}\, \mathrm{d}x \qquad (9)$$

Convolution, or folding, is a basic concept in crystallography that is particularly important in powder diffraction analysis. The process of convolution is one in which the product of two functions $f(x)$ and $g(x)$ is integrated over all space:

$$h(x') = \int_{-\infty}^{\infty} f(y)\, g(x' - y)\mathrm{d}y = f \circ g, \qquad (10)$$

where $h(x')$ is the convolution product, $y$ is the variable of integration in the same domain as $x'$, and $\circ$ denotes the convolution process. Convolution can be understood as "blending" one function with another, producing a kind of very general "moving average" (see Weisstein (2021) for definition and animated examples) Most functions cannot be convoluted analytically and the convolution integral needs to be calculated numerically.

An alternative way of calculation follows from the convolution theorem of Fourier transformation. The Fourier transform of the convolution function can be calculated by

$$\begin{aligned} \int_{-\infty}^{\infty} h(x')\mathrm{e}^{2\pi \mathrm{i} s x'}\, \mathrm{d}x' &= \int_{-\infty}^{\infty}\int_{-\infty}^{\infty} f(y)\, g(x' - y)\mathrm{d}y\, \mathrm{e}^{2\pi \mathrm{i} s x'}\mathrm{d}x' \\ &= \int_{-\infty}^{\infty}\int_{-\infty}^{\infty} f(y)\, g(x' - y)\mathrm{d}y\, \mathrm{e}^{2\pi \mathrm{i} s (x' - y + y)}\mathrm{d}x', \end{aligned} \qquad (11)$$

which can be rewritten by using the substitution $u = x' - y$ and therefore $\mathrm{d}u = \mathrm{d}x'$ as

$$\begin{aligned} &= \int_{-\infty}^{\infty}\int_{-\infty}^{\infty} f(y)\, g(u)\mathrm{e}^{2\pi \mathrm{i} s y}\mathrm{d}y\, e^{2\pi \mathrm{i} s u}\mathrm{d}u \\ = \int_{-\infty}^{\infty}\int_{-\infty}^{\infty} f(y) e^{2\pi \mathrm{i} s y}\mathrm{d}y\, g(u) e^{2\pi \mathrm{i} s u}\mathrm{d}u &= F(s)\, G(s). \end{aligned} \qquad (12)$$

From the latter, it follows directly that the Fourier transform of the convolution integral is the product of the Fourier-transforms of all functions participating in the convolution:

$$f \circ g \leftrightarrow F(s)\, G(s), \qquad (13)$$

while the back-transformation of a convolution is the product of the back-transformed functions, which participate in the convolution:

$$f(x)\ g(x) \leftrightarrow F \circ G. \tag{14}$$

In many cases, an analytic Fourier transformation of a mathematical function is not possible, requiring the numerical Fourier transformation of a finite list of N function values $u(r)$ at index r (running from 1 to N), which are separated by a constant step width $\Delta x$. The corresponding running index in Fourier space is s (running from 1 to N) and the Fourier transformed values are separated by a constant step width $\Delta s$. This means that some piece of the integral can be discretised by

$$x \to x_1 + (r-1)\Delta\mathrm{x} \quad \text{and } s \to (s-1)\Delta\mathrm{s} \tag{15}$$

with

$$\Delta x \Delta s = \frac{1}{N} \tag{16}$$

leading to

$$\begin{aligned} &f(x) \to f(x_1 + (r-1)\Delta x) = f_r \text{ and} \\ &F(s) \to F\big((s-1)\Delta s\big) = F_s. \end{aligned} \tag{17}$$

Eq. 7 can thus be written in a discretized form as

$$\begin{aligned} F_s &= \sum_{r=1}^{N} f_r \mathrm{e}^{2\pi\mathrm{i}(s-1)\Delta s[x_1+(r-1)\Delta x]}\,\Delta x \\ &= \sum_{r=1}^{N} f_r \mathrm{e}^{2\pi\mathrm{i}(s-1)\Delta s x_1} \mathrm{e}^{2\pi\mathrm{i}(s-1)\Delta s[(r-1)\Delta x]}\,\Delta x \\ &= \sum_{r=1}^{N} f_r \mathrm{e}^{2\pi\mathrm{i}(s-1)x_1/(N\Delta x)} \mathrm{e}^{2\pi\mathrm{i}(s-1)[(r-1)/N]}\,\Delta x.^{3} \end{aligned} \tag{18}$$

## Probability density functions

The shape of powder diffraction peaks is usually described by individual or convoluted probability density functions (PDFs) used to describe statistical processes. In statistics, PDFs are characterized by

[3] In Mathematica, a numerical discrete Fourier transformation is defined as $F_s = \frac{1}{\sqrt{N}} \sum_{r=1}^{N} u_r \mathrm{e}^{2\pi\mathrm{i}(r-1)(s-1)/N}\,\Delta x$ from which follows that the $f_r$ values must be multiplied by a complex phase factor: $u_r = f_r \sqrt{N} \mathrm{e}^{2\pi\mathrm{i}(s-1)x_1/(N\Delta x)}$ (mathematica stackexchange questions 1714).

their moments, which are quantitative measures related to their shape. The zeroth moment is the total probability (which equals one), the first moment is the expected value (mean), the second central moment is the variance, the third standardized moment is the skewness, and the fourth standardized moment is the kurtosis. The variance is the expectation of the squared deviation of a random variable from its mean. Skewness is a measure of the asymmetry of the probability distribution of a real-valued random variable about its mean, and kurtosis is a measure of the "tailedness" of the probability distribution of a real-valued random variable (from Wikipedia).

In powder diffraction, the width of distributions used to describe peak profiles are either the standard deviation ($\sigma$), the full width at half maximum (fwhm) which is the difference between the two values of the independent variable at which the dependent variable is equal to half of its maximum value (height of the peak), the half width at half maximum (*hwhm*) which is fwhm/2, or the integral breadth ($\beta$), the latter being the width of a rectangle of identical height and area as the peak.

The standard deviation $\sigma$ or square root of the variance of a distribution described by $f(x)$ (which is normalized to an area of unity) is given as

$$\sigma = \sqrt{\langle(\Delta x - \langle x\rangle)^2\rangle} = \sqrt{\int_{-\infty}^{\infty}(x - \langle x\rangle)^2 f(x)dx}\,, \qquad (19)$$

and the average is given as

$$\langle x\rangle = \int_{-\infty}^{\infty} x f(x)dx, \qquad (20)$$

which agrees (in the case of a symmetric unimodal distribution) with the peak maximum $x_0$. For many common distributions, the variance and therefore the standard deviation are not defined. In these cases, always the *hwhm, fwhm,* or $\beta$ are used. The latter is defined as

$$\beta = \frac{1}{f(x_0)} \qquad (21)$$

for a function $f(x)$ that is normalized to an area of unity.

**Gaussian distribution**

The Gaussian (or normal) distribution is a very common distribution. Physical quantities expected to be the sum of many independent processes (such as measurement errors) often have distributions that are nearly normal. A Gaussian function normalized to an area of unity centred at a mean or expectation value $X_0$ is (Fig. 1 left) :

$$g(x') = \frac{1}{\sigma\sqrt{2\pi}}\,\mathrm{e}^{-\frac{1}{2}\left(\frac{x'}{\sigma}\right)^2} \qquad (22)$$

where $\sigma$ is the standard deviation and $\sigma^2$ the variance. The pre-factor follows from normalization:

$$\int_{-\infty}^{+\infty} g(x')\,\mathrm{d}x' = 1. \qquad (23)$$

The $hwhm_{\mathrm{G}}$ of a Gaussian is given by

$$hwhm_{\mathrm{G}} = \sqrt{2\ln 2}\sigma \approx 1.18\,\sigma. \qquad (24)$$

With $hwhm_{\mathrm{G}}$ as the width parameter, the definition of the Gaussian changes accordingly to

$$g(x') = \frac{\sqrt{\pi \ln 2}}{hwhm_{\mathrm{G}}\,\pi} \mathrm{e}^{-\ln 2\left(\frac{x'}{hwhm_{\mathrm{G}}}\right)^2}. \qquad (25)$$

The integral breadth of a Gaussian is given by:

$$\beta_{\mathrm{G}} = \sqrt{\frac{\pi}{4\ln 2}}\, fwhm_{\mathrm{G}} = \sqrt{2\pi}\sigma, \qquad (26)$$

The normalized Fourier transform (maximum value is 1) of a Gaussian function is itself a Gaussian function (Fig. 1 right):

$$G(s) = \mathrm{e}^{-2\pi^2 s^2 \sigma^2} \qquad (27)$$

with a full width at half maximum of

$$fwhm_{FTG} = \frac{\sqrt{2\ln 2}}{\pi\sigma}. \qquad (28)$$

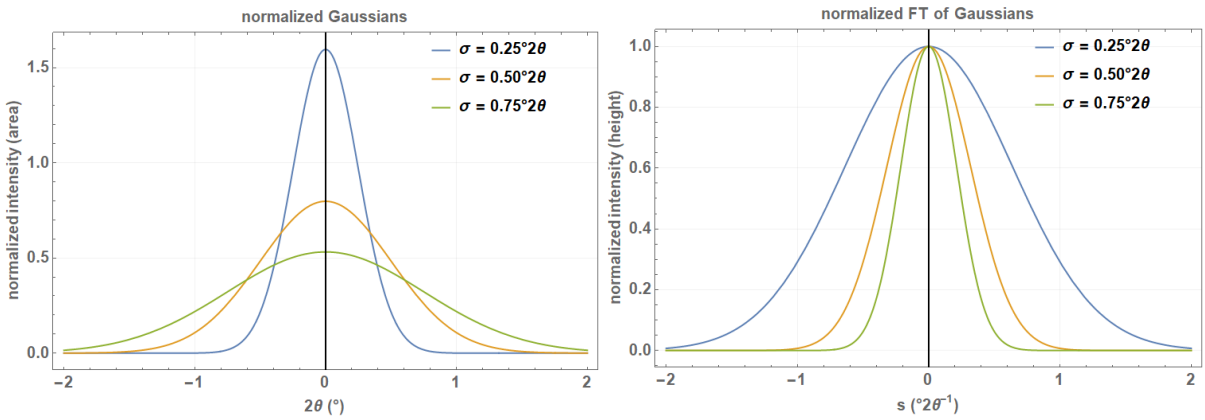


*Fig. 1: Series of normalized Gaussians (left) and their corresponding Fourier transforms (right) with different standard deviation σ on a 2θ- and reciprocal 2θ-scale.* The convolution of a Gaussian (1) with another Gaussian (2) is a Gaussian with the following property:

$$fwhm_{\mathrm{G}}^2 = fwhm_{\mathrm{G},1}^2 + fwhm_{\mathrm{G},2}^2\,, \qquad (29)$$

which follows directly form the additivity of variances and also holds for integral breadths.

**Lorentz distribution**

The Lorentz (or Cauchy) function is another important continuous probability density distribution, which might be attributed e.g. to the lifetime broadening of the characteristic X-ray emission line. The Lorentz function is used e.g. to describe the emission profile from an X-ray tube, the peak profile in some faulting problems when a random probability exists in the stacking sequence, as well as to approximate crystallite size and strain effects from the sample. Also in a perfect infinite crystal, Bragg peaks are not δ-functions, but finite Lorentzians with the *fwhm* being the Darwin width (Warren, 1990). The Lorentz distribution normalized to unity is defined as (Fig. 2 left)

$$l(x') = \frac{1}{\pi\left(\delta + \frac{x'^2}{\delta}\right)}, \qquad (30)$$

with δ being the Lorentzian half width at half maximum $hwhm_{\mathrm{L}}$. The Lorentz distribution is an example of a distribution with **no** mean, **no** standard deviation, **no** variance or higher moments defined. Its mode and median (the value separating the higher half from the lower half of a data sample) are well defined and are both equal to $X_0$.

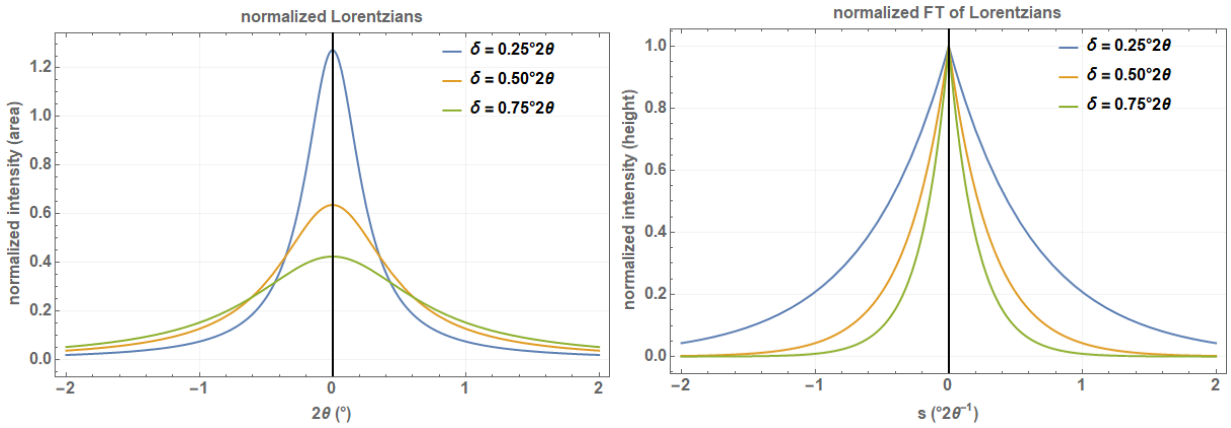


*Fig. 2: Series of normalized Lorentzians (left) and their corresponding real Fourier transforms (right) with different $\delta$ (=hwhm$_L$) on a 2$\theta$- and reciprocal 2$\theta$-scale.*

The integral breadth of a Lorentzian is given as:

$$\beta_{\mathrm{L}} = \frac{\pi}{2} fwhm_{\mathrm{L}} = \pi\delta. \qquad (31)$$

The real part of the Fourier transform (normalized to unity) of a Lorentzian is (Fig. 2 right)

$$L(s) = \mathrm{e}^{-2\pi\delta|s|}, \qquad (32)$$

with a full width at half maximum of

$$fwhm_{FTL} = \frac{\ln 2}{\delta\,\pi} \qquad (33)$$

The convolution of a Lorentzian (1) with another Lorentzian (2) is a Lorentzian with the following property:

$$fwhm_{\mathrm{L}} = fwhm_{\mathrm{L},1} + fwhm_{\mathrm{L},2}\,, \qquad (34)$$

which also holds true for integral breadths.

**The Voigt distribution**

The Voigt distribution, named after the German physicist Woldemar Voigt (Voigt, 1912) can be regarded as the convolution of a normalized Gaussian and a normalized Lorentzian:

$$v(x') = g(x') \circ l(x'). \qquad (35)$$

No analytical solution exists for the convolution integral, but it can be expressed by the real part of the complex error function for which good approximations exist (Fig. 3, left):

$$v(x') = \frac{\mathrm{Re}[w(z)]}{\sigma\sqrt{2\pi}} \qquad (36)$$

where $w(z)$ is called Faddeeva-function (also called Kramp-function or relativistic plasma-dispersion-function), and is a scalable complex conjugated error function. This is given by

$$w(z) = e^{-z^2}\mathrm{erfc}(-\mathrm{i}z) = e^{-z^2}\left(1 + \frac{2\mathrm{i}}{\sqrt{\pi}}\int_0^z e^{t^2}\,\mathrm{d}t\right), \qquad (37)$$

and the argument z is

$$z = \frac{x' + \mathrm{i}\delta}{\sigma\sqrt{2}}. \qquad (38)$$

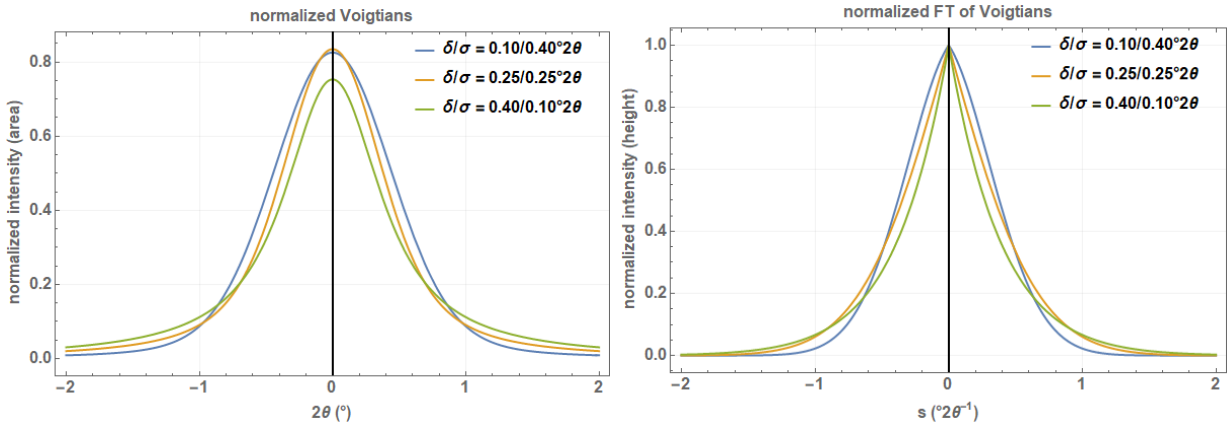


*Fig. 3: Series of normalized Voigt profiles (left) and their corresponding real Fourier transforms (right) with different Gaussian standard deviation $\sigma$ and Lorentzian hwhm $\delta$ on a $2\theta$- and reciprocal $2\theta$-scale.*

When the results of a series of measurements are described by a normal distribution with standard deviation $\sigma$ and expected value 0, then

$$\operatorname{erf}\left(\frac{a}{\sigma\sqrt{2}}\right) \tag{39}$$

is the probability that the error of a single measurement lies between −a and +a, for positive a. The error function is defined as (Fig. 4):

$$\operatorname{erf}(x) = \frac{2}{\sqrt{\pi}} \int_0^x \mathrm{e}^{-t^2}\,\mathrm{d}t. \tag{40}$$

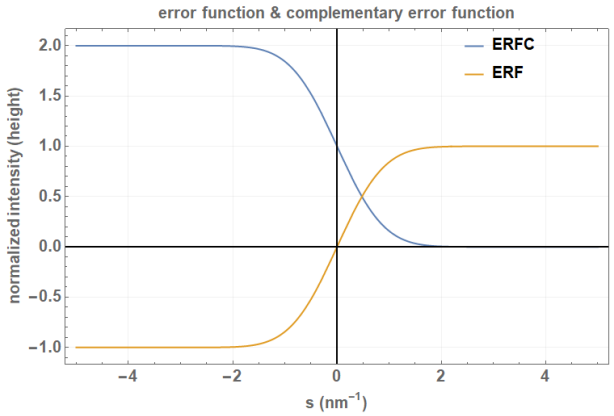


*Fig. 4: Plot of the error function and the complimentary error function given in Eqs. (38) and (39) (from Dinnebier et al., 2018).*

The complementary error function is defined as

$$\mathrm{erfc}(x) = 1 - \mathrm{erf}(x) = \frac{2}{\sqrt{\pi}} \int_x^\infty e^{-t^2}\, \mathrm{d}t. \qquad (41)$$

The $fwhm_v$ of a Voigt function can be reasonably approximated either by (*Olivero & Longbothum, 1977)* (Fig. 5)

$$fwhm_V \approx 0.5346\, fwhm_L + \sqrt{0.2166\, {fwhm_L}^2 + {fwhm_G}^2} \qquad (42)$$

or by a polynomial of 5th order (Thompson, Cox, Hastings, 1987):

$$\begin{aligned} fwhm_v \approx \big( & fwhm_{\mathrm{g}}^5 + 2.69269 fwhm_{\mathrm{g}}^4 fwhm_{\mathrm{l}} \\ & + 2.42843 fwhm_{\mathrm{g}}^3 fwhm_{\mathrm{l}}^2 \\ & + 4.47163 fwhm_{\mathrm{g}}^2 fwhm_{\mathrm{l}}^3 \\ & + 0.07842 fwhm_{\mathrm{g}} fwhm_{\mathrm{l}}^4 + fwhm_{\mathrm{l}}^5 \big)^{1/5}. \end{aligned} \qquad (43)$$

The integral breadth of a Voigt function is given as (Schoening, 1965)

$$\beta_{\mathrm{V}} = \beta_{\mathrm{G}} \frac{\mathrm{e}^{-k^2}}{\mathrm{erfc}\,(k)}, \qquad (44)$$

with the so-called characteristic breadth ratio of a Voigtian *k*:

$$k = \frac{\beta_{\mathrm{L}}}{\sqrt{\pi}\beta_{\mathrm{G}}}. \qquad (45)$$

The Fourier transform of the Voigt function can be written as (Fig.3, right)

$$V(s) = \mathrm{e}^{-2\delta|\pi \mathrm{s}| - 2\sigma^2(\pi \mathrm{s})^2} = \mathrm{e}^{-2\beta_L|\mathrm{s}| - \pi\beta_G^2 \mathrm{s}^2} \qquad (46)$$

with a full width at half maximum of

$$fwhm_{FTV} = \frac{-\delta + \sqrt{\delta^2 + \sigma^2 \ln 4}}{\sigma^2 \pi}. \qquad (47)$$

The convolution of two Voigt functions again is a Voigt function, a property which is used e.g. in the concept of the so-called double-Voigt approach where two Voigtians are convoluted each having its own Gaussian and Lorentzian fractions (Balzar, 1999).

For a long time, the exact computation of a Voigt profile was computationally expensive. One way to approximate a given Voigt function is to use a linear combination of a Gaussian and a Lorentzian, called the pseudo-Voigt approximation:

$$pv(x') = \eta\, l(x') + (1 - \eta)\, g(x'). \qquad (48)$$

The mixing parameter $\eta$ can be calculated using Eq. 43 in the range $0 \leq \eta \leq 1$ by a cubic polynomial leading to the TCH (Thompson-Cox-Hastings) pseudo-Voigt function (Thompson et al., 1987):

$$\eta = 1.36603\, fwhm_l/fwhm_v - 0.47719(fwhm_L/fwhm_v)^2 + 0.11116(fwhm_L/fwhm_v)^3, \quad (49)$$

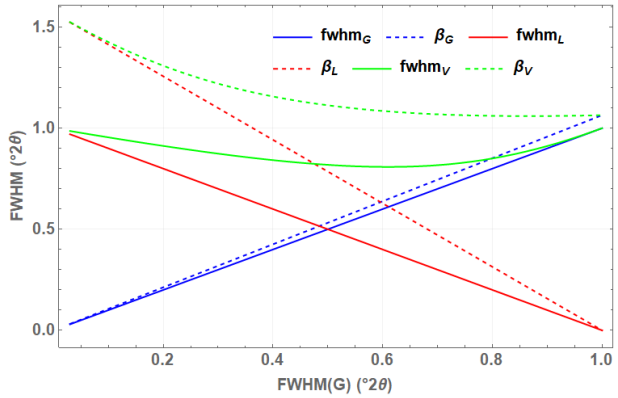


*Fig. 5: Plot of the fwhm of the TCH-Pseudo-Voigt function as a function of the fwhm's of the Gaussian and the Lorentzian part (solid lines) and the corresponding integral breadths $\beta$ (dashed lines).*

If a purely empirical approximation of a Voigt is needed (as is generally sufficient for the determination of the *IRF*), a simplified version of the pseudo-Voigt function can be used:

$$pv(x') = \frac{(1-\eta)}{hwm_v\,\pi}\sqrt{\pi \ln 2}\, e^{-\ln 2\left(\frac{x'}{hwm_v}\right)^2} + \frac{\eta}{hwm_v\,\pi}\frac{1}{1+\left(\frac{x'}{hwm_v}\right)^2} \quad (50)$$

with its Fourier transform:

$$PV(s) = (1-k)e^{-\frac{\pi^2 hwm_v{}^2 s^2}{\ln 2}} + k e^{-2\,\pi\, hwm_v\, s}, \qquad k = \left[1 + \frac{1-\eta}{\eta\sqrt{\pi \ln 2}}\right]^{-1}. \quad (51)$$

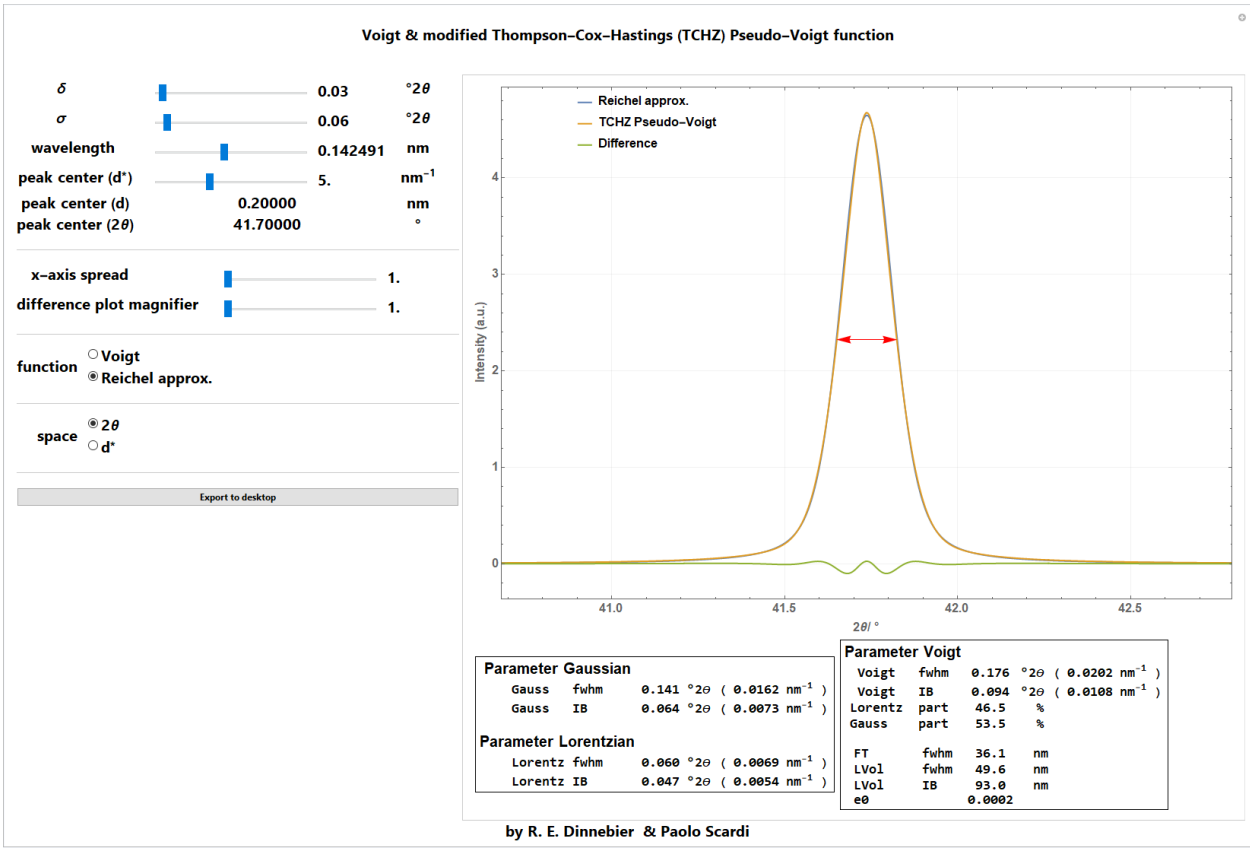


*Fig. 6: Screenshot of a Mathematica script for comparing the pure Voigt profile, the Reichel approximation and the TCH-Pseudo-Voigt profile for a given Gaussian standard deviation and Lorentzian hwhm in 2θ or d* space. Values for crystallite size and microstrain were calculated using the formulas by Balzar (1999) under the assumption that the entire width of the peak is caused by either one.*[4]

Among the many approximation functions of the Voigt function found in literature over time, the one by Chiarella and Reichel (1968) which was later modified by Abrarov *et al.* (2012) is a good compromise regarding speed and accuracy (Figs. 6 & 7):

$$w(z) \approx i\,\frac{h}{\pi\, z} - i\frac{2\,h\,z}{\pi}\sum_{n=1}^{N}\frac{e^{-n^2h^2}}{n^2h^2 - z^2} \qquad (52)$$

with $h = \frac{\pi}{\tau_m}$, and the chosen parameters $\tau_m$ and $n$ which determine the degree of approximation (typically $\tau_m$ = 12 and $n$ = 23). This function can be efficiently compiled in Mathematica, increasing the speed of computation considerably (Mathematica Stack Exchange question 19884). Since the difference between a Voigt profile and the Chiarella and Reichel approximation is negligible (Fig. 7), the latter is used throughout the Mathematica scripts if a Voigt profile is required.

[4] A good explanation how size and strain values are calculated from the *fwhm* or the *IB* of a Voigt function in the TOPAS (Coelho, 2018) software, is given by Evans (2021).

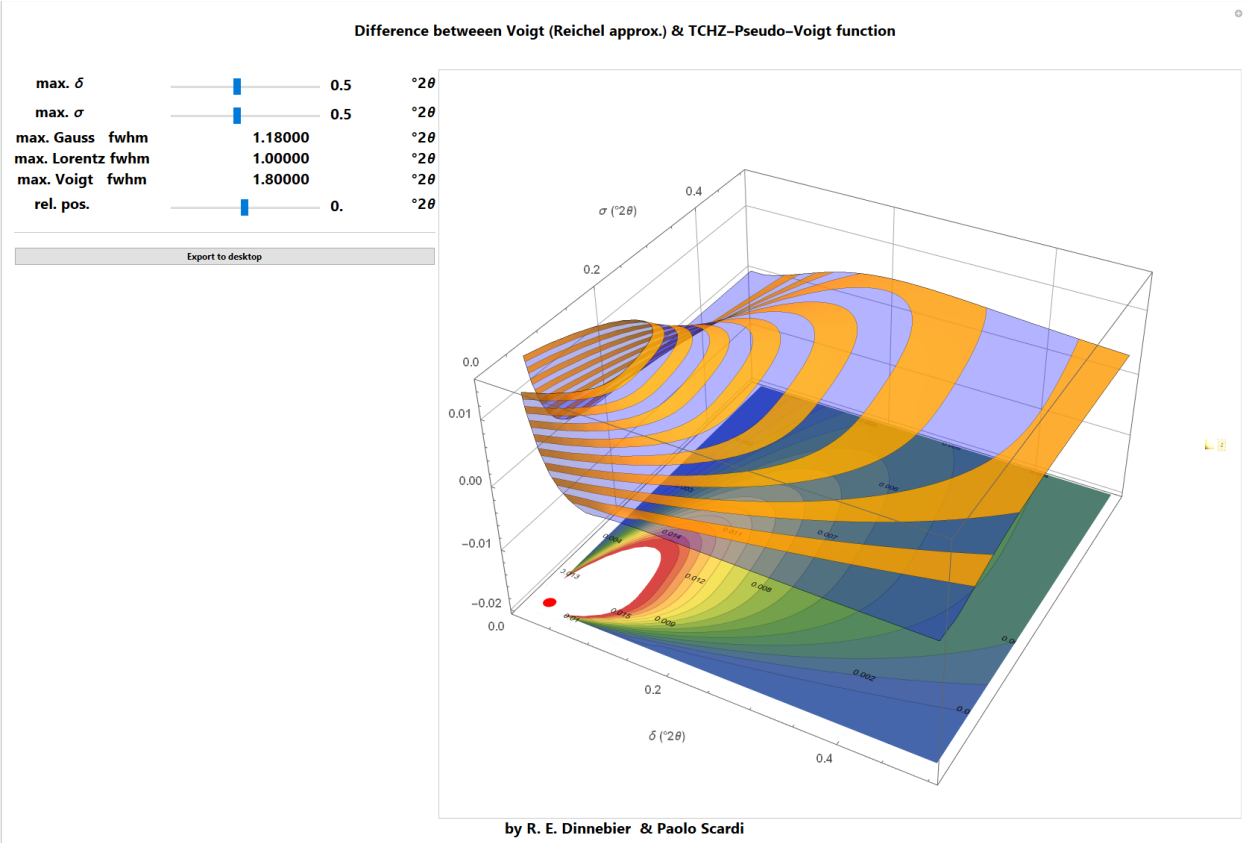


*Fig. 7: Screenshot of a Mathematica script for comparing the Reichel approximation of the Voigt function with the TCH-Pseudo-Voigt profile* as a function of *Gaussian standard deviation and Lorentzian hwhm at a given position relative to the peak centre in 3-D.*

The dependence of the Gaussian $fwhm_G$ and Lorentzian $fwhm_L$ on the $2\theta$-diffraction angle is usually described by low order polynomials as a function of $\cos\theta^{-1}$ and $\tan\theta$. While the $\cos\theta^{-1}$ dependence follows directly from the Scherrer equation (Scherrer, 1918) and is attributed to the size of coherently scattering domains (often denoted as crystallite size), the $\tan\theta$ dependence is a measure for microstrain and can be derived from the full derivative of the Bragg equation (Bragg & Bragg, 1913). In an empirical but flexible way, the Gaussian $fwhm_G$ and Lorentzian $fwhm_L$ are often defined as (Thompson *et al*., 1987, Young, 1993)

$$fwhm_G = \sqrt{U\tan^2\theta + V\tan\theta + W + \frac{Z}{\cos^2\theta}} \qquad (53)$$

$$fwhm_L = X\tan\theta + \frac{Y}{\cos\theta},$$

where U, V, W, X, Y, Z are refineable parameters. Apparently, the parameters have been chosen in a way that U and X are somehow related to microstrain while Z and Y are kind of related to domain size (VonDreele, 2008) (Fig. 8). Refining all parameters simultaneously generally leads to over-parameterization and high correlation, destabilizing the optimization process.

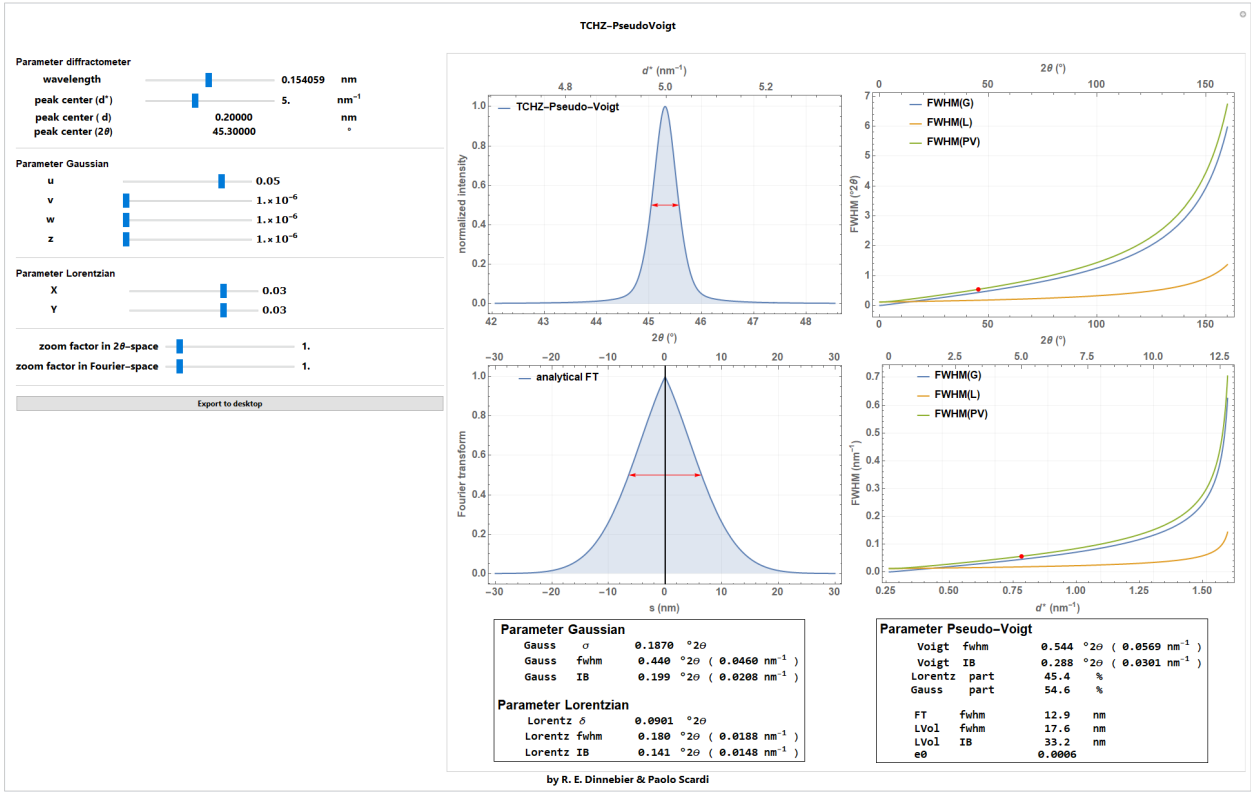


*Fig. 8: Screenshot of a Mathematica script for visualisation of the dependence of the TCH-Pseudo-Voigt function and its Fourier transform on the diffraction angle. Values for crystallite size and microstrain were calculated using the formulas by Balzar (1999) under the assumption that the entire width of the peak is caused by either one.*

In order to retrieve the width parameters of a Voigt function, which is blurred by Poisson noise, a variety of least squares algorithms (e.g. gradient, Levenberg-Marquardt, Newton) is available (Press *et al.*, 2007). A Mathematica script has been written to evaluate the reliability of parameter retrieval depending on the amount of noise and to determine the degree of correlation between the fitting parameters (Fig. 9). The script is a useful tool to test and visualize data quality and the effect of noise on the refined parameters, applying different algorithms of minimization. It also introduces the concept of estimated standard deviation.

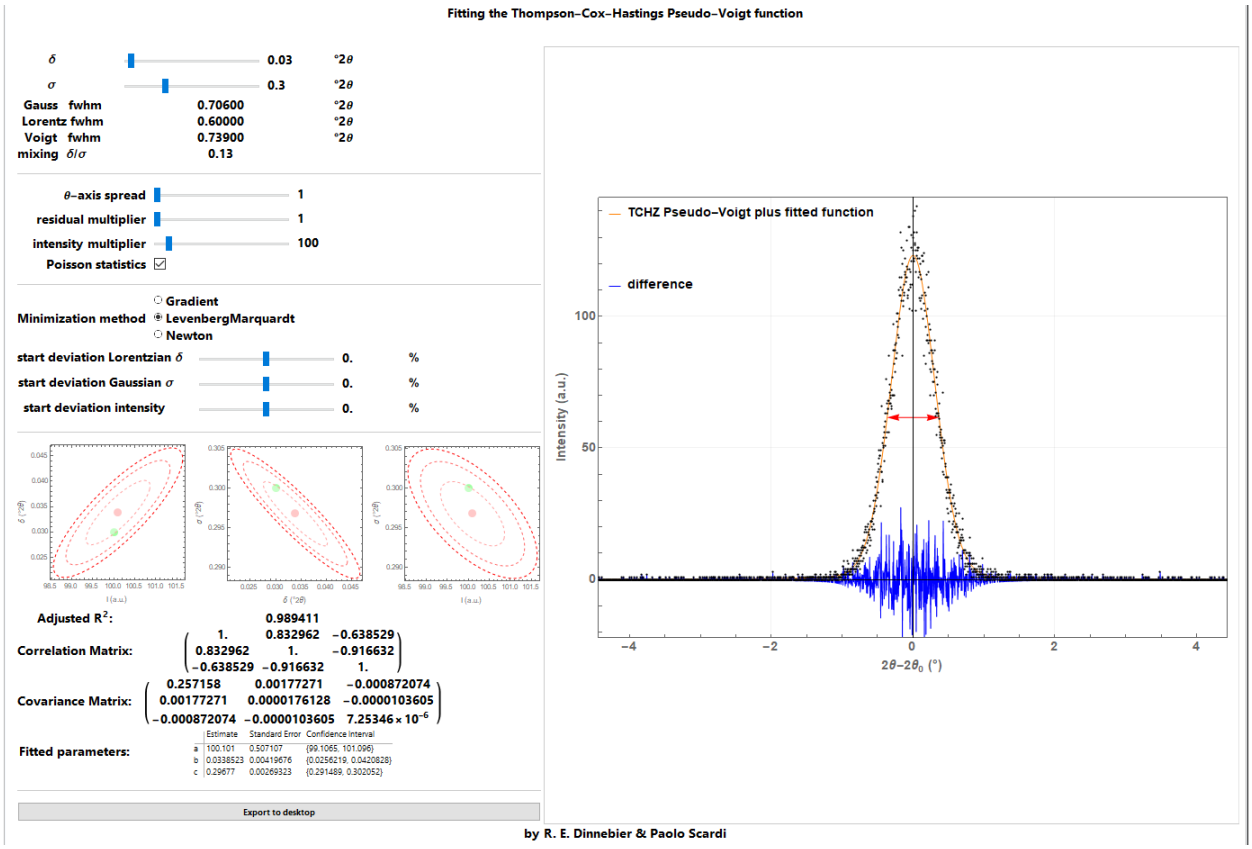


*Fig. 9: Screenshot of a Mathematica script for visualisation of least squares fitting using different algorithms of the TCH-Pseudo-Voigt perturbed by Poisson noise.*

## Instrumental aberrations to the peak profile

Only in a few cases, the IRF can be fully described using a symmetrical Voigt-like profile function. In particular, the curvature of the Debye-Scherrer rings introduces a certain amount of asymmetry due to axial divergence if a rectangular receiving slit or silicon strip is cutting out only a small part of the ring. Each element in the optical pathway of the incident and diffracted beam convolutes its characteristic shape into the peak profile. The functions to describe the effects are either highly sophisticated based on physics and geometry, purely empirical, or a mixture of both. They are convoluted in real space, or multiplied in Fourier space, into the existing peak profile. In the following, a selection of four simple aberration functions in powder diffraction, which have proven to be useful, are discussed. Although this chapter is restricted to instrumental aberrations, the asymmetry introduced by the transparency effect, which depends on the preparation technique is included since it is not related to the microstructure of the sample. It should be noted that all functions presented here can be found in the TOPAS software (Coelho, 2018).

**The box (hat) function**

Several instrumental aberrations in the equatorial plane of a diffractometer are commonly described by a box (sometimes called top-hat) function. These include the width of the source, the thickness of sample surface as projected onto the equatorial plane, the width of the receiving slit, the width of strips in position sensitive strip detectors, etc. The normalized (area under its graph is 1) box function with its width *a* defined as (Fig. 10, left)

$$\mathrm{box}(x') = \begin{cases} \frac{1}{a} \text{ for } -\frac{a}{2} < (x') < \frac{a}{2}. \\ else\ 0 \end{cases} \qquad (54)$$

At the extreme case of $a \rightarrow 0$, the box function turns into a $\delta$ function. For practical reasons this is achieved by setting *a* to a value < $10^{-5}$.

The normalized (maximum value is 1) Fourier transform of a box function with the reciprocal variable *s* is a real function calculated as (Fig. 10, right):

$$\mathrm{BOX}(s) = 2\frac{\sin(s\,a/2)}{s\,a} \qquad (55)$$

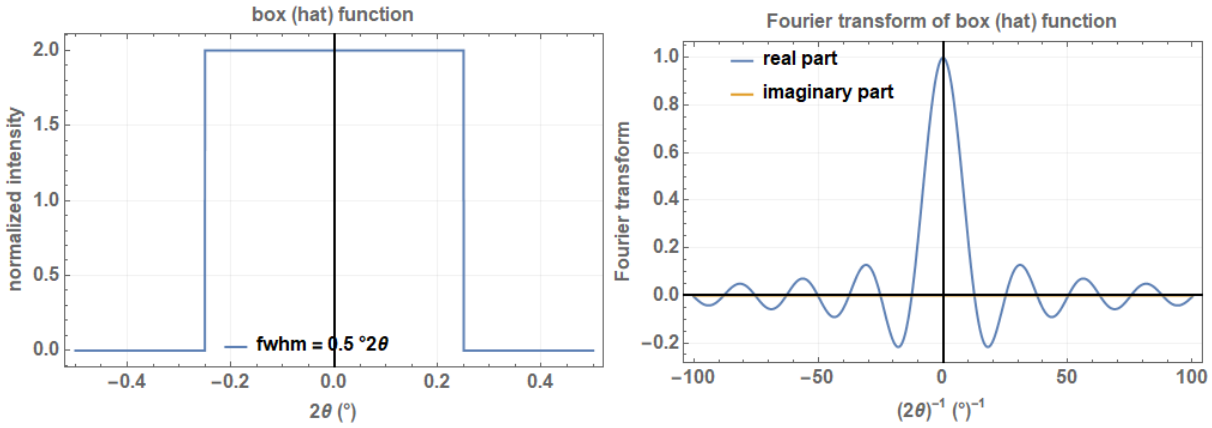


*Fig. 10: The box function on a $2\theta$ scale with a width of 0.5° $2\theta$ (left) and its real Fourier transform (right).*

The convolution of a box function with itself leads to the triangular function. If the convolution process is repeated, the convoluted function approaches a Gaussian. In practice, this is realized after 5 or more convolutions.

To mimic the transmittance of a rectangular slit on the °2θ with a width of *c* in mm (typically on the order of 0.1 mm) or the width of source in the equatorial plane of a diffractometer with a secondary radius $Rs$ in mm, a constant function for calculating the *fwhm a* of the box function is used (Fig. 11):

$$a(2\theta) = \frac{180}{\pi}\frac{c}{Rs}. \qquad (56)$$

In order to calculate the width (*fwhm*) of the box function in ° for the so called specimen tilt, the following function is used (Fig. 11):

$$a(2\theta) = \frac{180}{\pi}\frac{c\cos\theta}{Rs}. \qquad (57)$$

where c (in mm) represents the "thickness" of the sample surface as projected onto the equatorial plane (Cheary & Coelho, 1992).

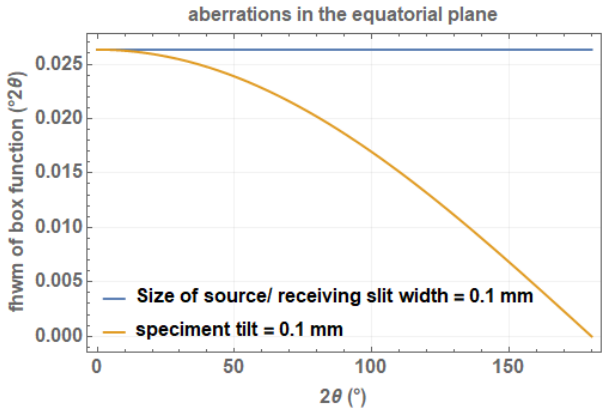


*Fig. 11: Aberrations in the equatorial plane of a diffractometer assuming a secondary radius of 217.5 mm, a slit width (either receiving slit or size of source) and a specimen tilt of 0.1 mm as a function of diffraction angle 2*θ.

In case an equatorial aberration is non-symmetrical (like for tube tails which might have different lengths on each side), a normalized half box function acting either on the left or the right side of a diffraction peak can be defined as (Fig. 12, left)

$$\mathrm{halfbox}(x') = \begin{cases} \frac{1.}{|a|} & (a < 0 \wedge x' < 0 \wedge x' > a) \vee (a > 0 \wedge x' > 0 \wedge x' < a) \\ else\ 0 \end{cases}, \qquad (58)$$

with its normalized complex Fourier transform (Fig. 12, right):

$$\mathrm{HALFBOX}(s) = \frac{\mathrm{i} - \mathrm{i}\, e^{i\,s\,a}}{\mathrm{s}\ a}. \qquad (59)$$

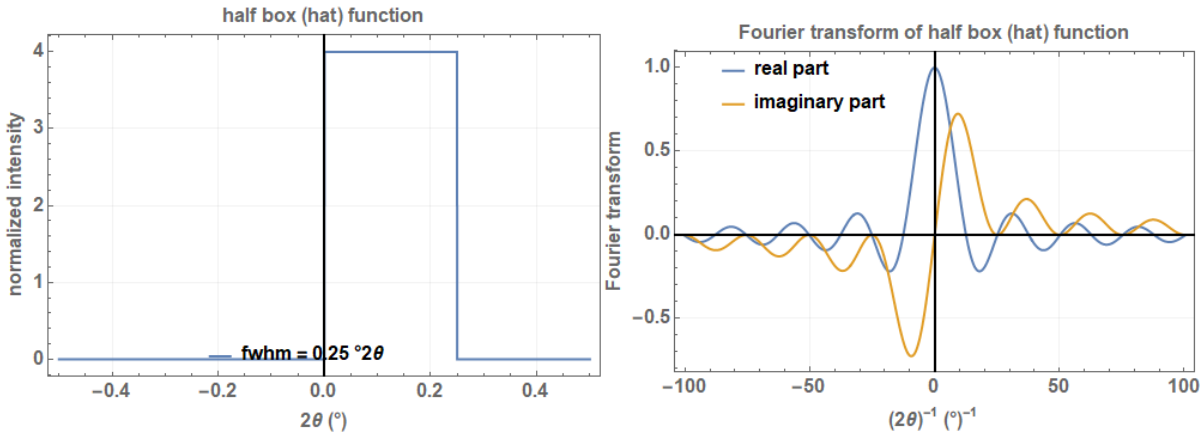


*Fig. 12: The half box function on a 2θ scale with a width of 0.25° 2θ (left) and its complex Fourier transform (right).*

To mimic the aberration caused by tube tails (Bergmann et a., 2000), a combination of a box function describing the tube filament width in mm and two half box functions with an effective width of tube tails in the equatorial plane perpendicular to the X-ray beam in negative and positive z-direction in mm can be used. An additional parameter defining the fractional height of the tube tails relative to the main beam is then needed (Fig. 13).

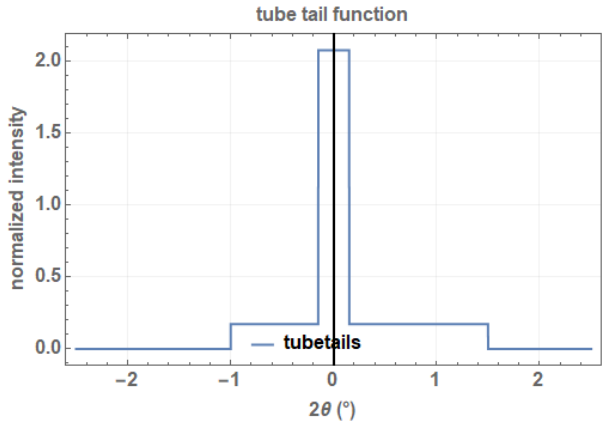


*Fig. 13: Tube tail function as a combination of a box function and two (left, right) half box functions for the tails.*

A screenshot of a Mathematica script where the box/half box function from different kinds of aberrations in the equatorial plane of the diffractometer is convoluted into a Voigt profile is shown in Fig. 14.

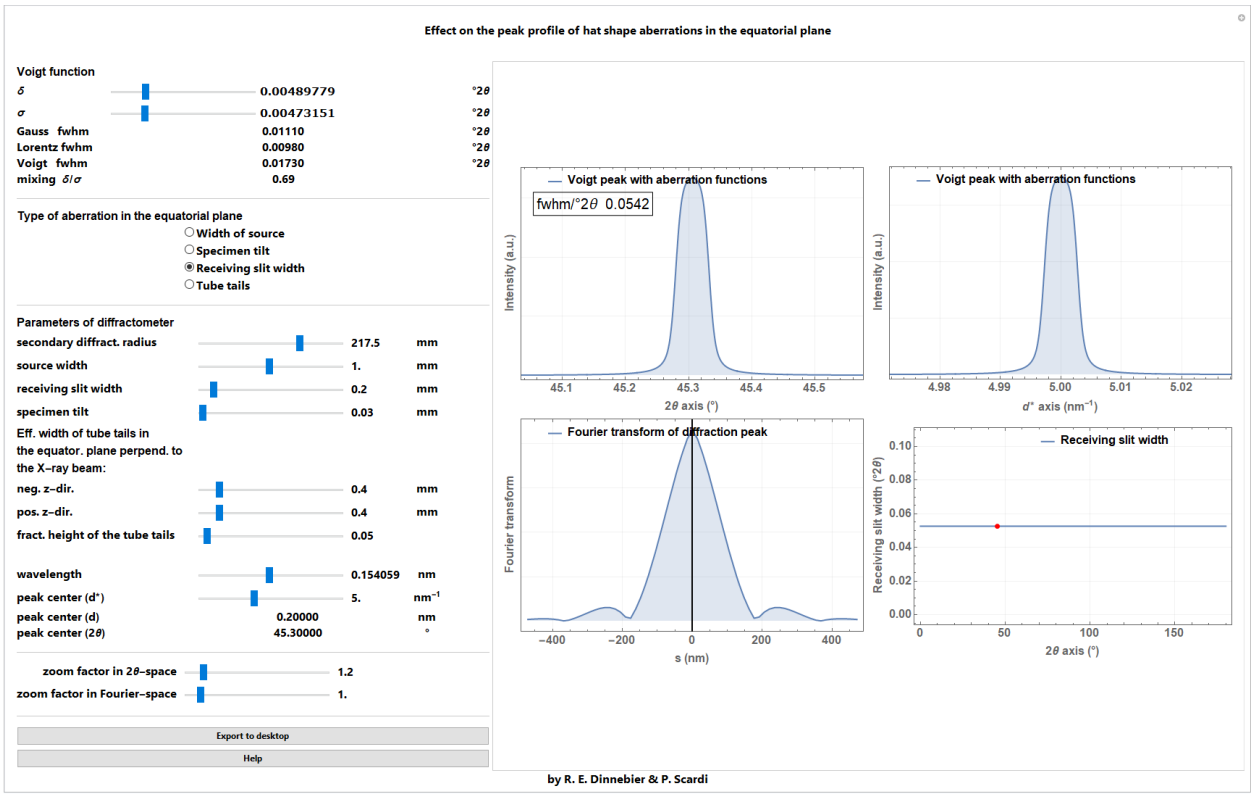


*Fig. 14: Screenshot of a Mathematica script dealing with the convolution of the box function into a Voigt profile. Different kinds of aberrations in the equatorial plane of a diffractometer assuming a secondary radius of 217.5mm, a slit width originating from a receiving slit or the size of the source, or from a specimen tilt as a function of diffraction angle 2θ can be selected.*

### The circles function

A simple approximate function for modelling the asymmetry of a Bragg reflection is the so-called circles function with the cut-off value $\varepsilon_m$ determining the curvature as adjustable parameter (Fig. 15 left):

$$\text{circles}(x') = \frac{\sqrt{\left|\frac{\varepsilon_m}{x'}\right| - 1}}{|\varepsilon_m|} \text{ for } 0 < x' \leq \varepsilon_m \; and \; |\varepsilon_m| > 0 \qquad (60)$$

One of the main applications for this function is the phenomenological modelling of the peak asymmetry caused by axial divergence, which is predominantly caused by the increasing curvature of the Debye-Scherrer rings at very low and extremely high angles which are cut by (typically) rectangular receiving slits of finite width (Cheary & Coelho, 1998). The complex Fourier transform of the circles function (Fig. 15 right) is defined as

$$\begin{aligned}&\text{CIRCLES}(s)\\&= 2({}_1F_2(0.25; 0.5{,}1.25; -0.25s^2{\varepsilon_m}^2)\\&+ 0.3325is\ \varepsilon_m\ {}_1F_2(0.75; 1.5{,}1.75; -0.25s^2{\varepsilon_m}^2))\\&+ \frac{i\left(-1+e^{is\ \varepsilon_m}\right)}{s\ \varepsilon_m},\end{aligned} \quad (61)$$

with the HypergeometricPFQ function ${}_1F_2$.

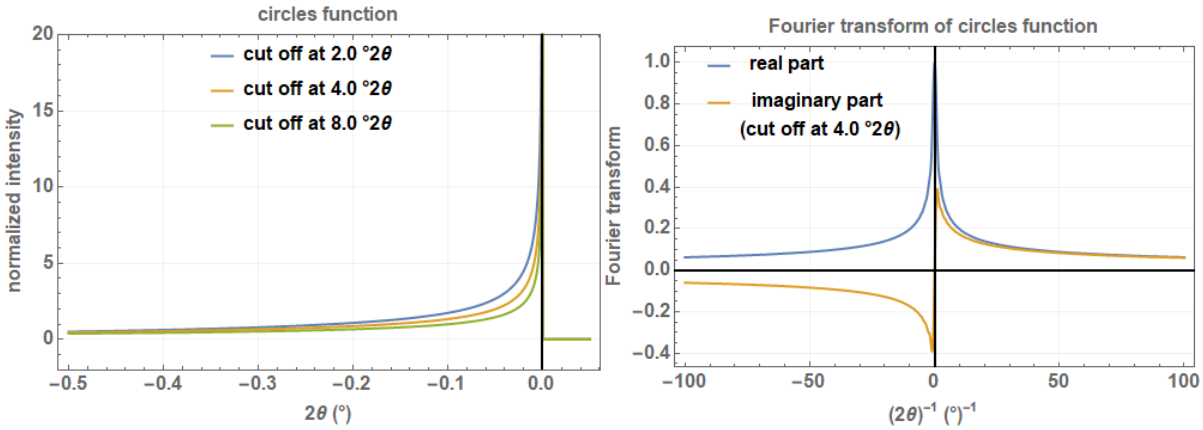


*Fig. 15: The circles function on a 2θ scale with three cut-off values of 2, 4, and 8° 2θ (left) and the Fourier transform of the circles function with a cut-off value of 4° 2θ showing the real and the imaginary part (right).*

In order to model axial divergence with the circles function for angular dispersive data, the angular dependence of the cut-off value $\varepsilon_m$ is well described by a tan(2θ)$^{-1}$ type of function of the receiving slit length *c* in mm. Please note that the asymmetry is reversed above 90° 2θ (actually closer to 120° 2θ as described in Cheary & Coelho, 1998) (Fig. 16):

$$a(2\theta) = -\frac{90}{\pi}\frac{c}{Rs^2\tan\theta} \quad (62)$$

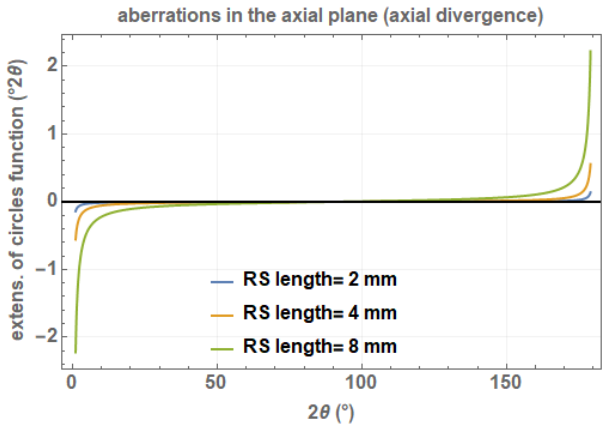


*Fig. 16: Cut-off values (= curvature) of the circles function to describe asymmetry due to axial divergence* as a function of *scattering angle for a diffractometer with a secondary radius of 217.5 mm and different receiving slit lengths in mm.*

More sophisticated functions to describe the asymmetry due to axial divergence of divergent beam diffractometers are found in literature. The mathematical formalism to describe peak asymmetry due to the finite size of the detector receiving slit and the curvature of the Debye-Scherrer rings for parallel beam geometry has been developed by Van Laar & Yelon (1984) and was implemented by Finger *et al.*, (1994). Extensions to cover divergent beam geometry, common for laboratory diffractometers, where also developed (e.g. Cheary & Coelho, 1998; Mendenhall *et al.*, 2017).

A screenshot of a Mathematica script where the circles function for describing asymmetry due to axial divergence of the diffractometer convoluted into a Voigt function is shown in Fig. 17.

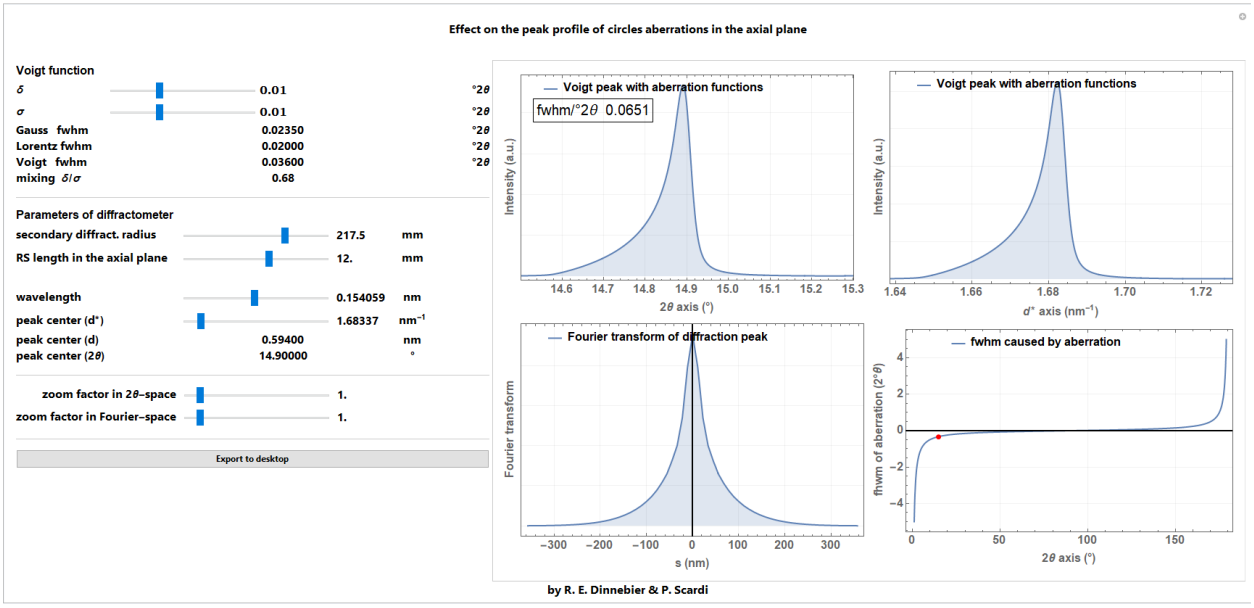

*Fig. 17: Screenshot of a Mathematica script dealing with the convolution of the circles function into a Voigt profile due to axial divergence caused by the length of a rectangular receiving slit.*

**1/x-function**

Another aberration function to describe certain types of asymmetry of a Bragg reflection is a so-called 1/x decay function defined as (Fig. 18, left)

$$oneonx(x') = \frac{1}{2\sqrt{|x'\varepsilon_m|}} \text{ for } 0 < x' \leq \varepsilon_m\,, \qquad (63)$$

where the parameter $\varepsilon_m$, which can be either positive or negative, is the cut-off value defining the extension of the asymmetric tail on the given length scale. The normalized complex Fourier transform of a 1/x function with the reciprocal variable *s* is calculated as (Fig. 18, right)

$$ONEONX(s) = \\ = \frac{1.25(\text{FresnelC}[\sqrt{\frac{2}{\pi}}\sqrt{s}\sqrt{\varepsilon_m}] + i\text{FresnelS}[\sqrt{\frac{2}{\pi}}\sqrt{s}\sqrt{\varepsilon_m}])}{\sqrt{s}\sqrt{\varepsilon_m}}, \qquad (64)$$

with the two Fresnel integrals:

$$\text{FresnelC(z)} = \int_0^z \cos\frac{\pi\, t^2}{2}\, dt \;\; and \;\; \text{FresnelS(z)} = \int_0^z \sin\frac{\pi\, t^2}{2}\, dt. \qquad (65)$$

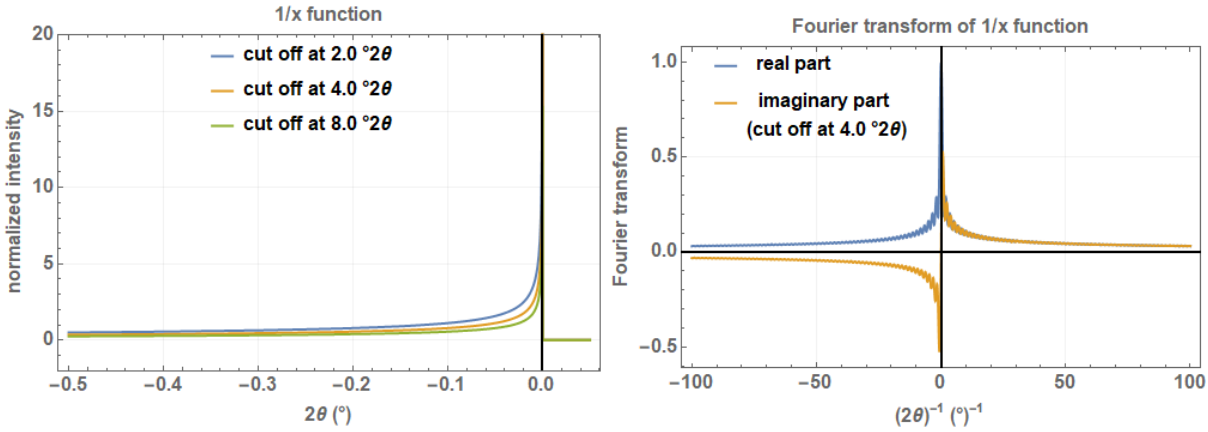


*Fig. 18: The 1/x function on a 2θ scale with three cut-off values of 2, 4, and 8° 2θ (left) and its Fourier transform with a cut-off value of 4° 2θ showing the real and the imaginary part (right).*

The 1/x function is mainly used for the phenomenological description of the equatorial divergence caused by a divergence slit (either fixed or variable) on the peak profile for angular dispersive data.

The cut-off value $\varepsilon_m$ as a measure for the peak asymmetry is calculated for a fixed or variable divergence slit as (Cheary et al., 2004):

$$\varepsilon_m(2\theta) = -\frac{180}{\pi}\left(\frac{c}{2\,Rs}\right)^2 \sin 2\theta. \qquad (66)$$

with the illuminated sample length *c* (in mm), which is constant if the divergence slit is variable, but depends on the opening angle α (in degrees) if the divergence slit is fixed (Fig. 19):

$$c = \frac{\pi}{180}\frac{\alpha\, Rs}{2}\left(\frac{1}{\sin\left(\theta - \frac{\alpha}{2}\right)} + \frac{1}{\sin\left(\theta + \frac{\alpha}{2}\right)}\right). \qquad (67)$$

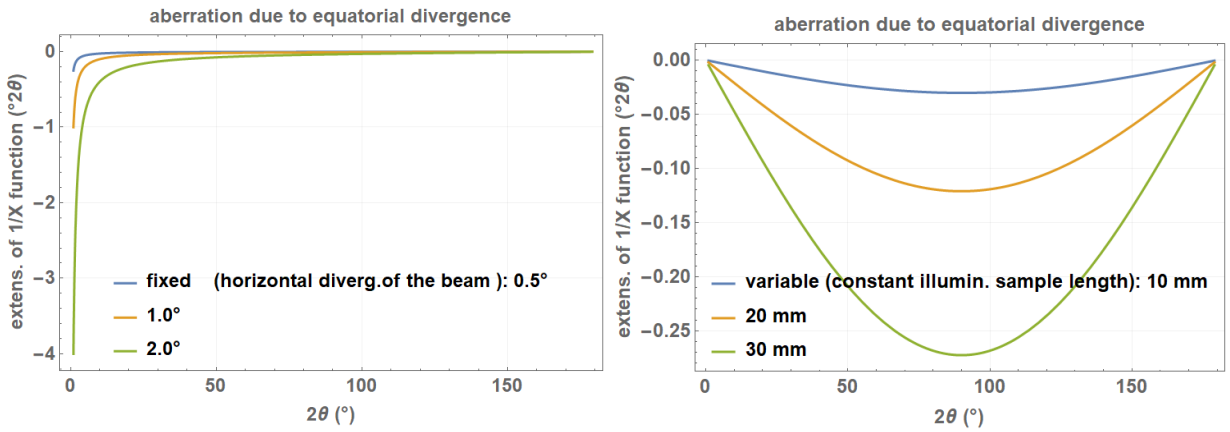


*Fig. 19: Angular dependence of the 1/x correction function for modelling the peak asymmetry due to equatorial divergence caused by a fixed divergence slit of 0.5°, 1.0°, or 2.0° opening (left) and a variable divergence slit with a constant illuminated sample length of 10 mm, 20mm, or 30 mm (right). The secondary diffractometer radius is set to of 217.5 mm.*

A screenshot of a Mathematica script where the 1/x function for describing asymmetry due to fixed or variable divergence slits of the diffractometer convoluted into a Voigt function is shown in Fig. 20.

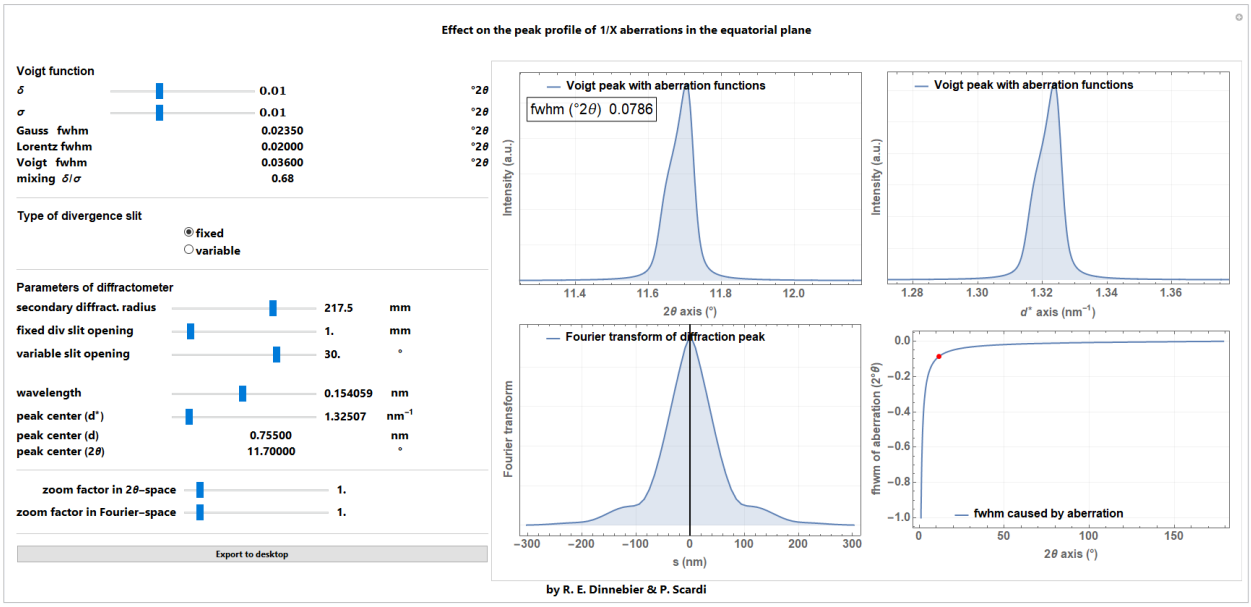


*Fig. 20: Screenshot of a Mathematica script dealing with the convolution of the 1/x correction function for modelling the peak asymmetry due to equatorial divergence caused by fixed or variable divergence slits.*

### The exponential function

Asymmetry of Bragg-reflections can also be described by a normalized exponential asymmetry decay function of the type (Fig. 21, left)

$$expo(x') = \frac{e^{\frac{x'}{\varepsilon_m}\ln 0.001}}{0.14462|\varepsilon_m|} \text{ for } 0 < x' \leq \varepsilon_m \qquad (68)^5$$

that is convoluted into the peak profile. The parameter $\varepsilon_m$, which can be either positive or negative, is the cut-off value which defines the extension of the asymmetric tail on the given length scale and is a measure for the degree of asymmetry. The normalized complex Fourier transform of the *expo* function with the reciprocal variable *s* is calculated as (Fig. 21, right)

$$EXPO(s) = \sqrt{2\pi}\frac{(2.7586i) - (0.0027586i)e^{i\,\varepsilon_m\,s}}{-\ln 0.001\;\; i + \varepsilon_m\, s}. \qquad (69)$$

5 ln(0.001) is a scaling factor which determines the value at $x' = \varepsilon_m$ to $\frac{0.001}{0.14462|\varepsilon_m|}$.

The exponential function can be useful for describing, e.g., the highly asymmetric instrumental peak shape of TOF data or the effects of transparency on the peak shape in Bragg-Brentano geometry.

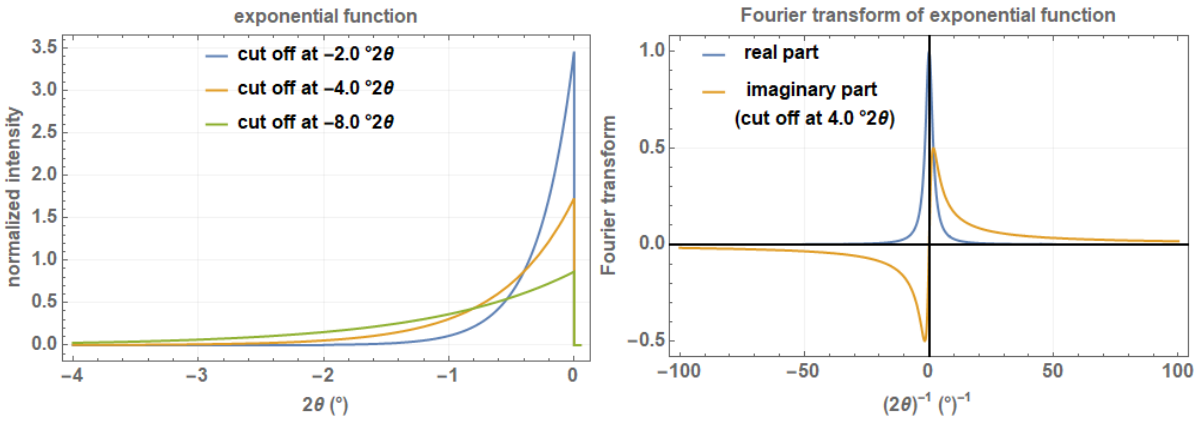


*Fig. 21: The exponential function on a $2\theta$ scale with three cut-off values of 2, 4, and 8° $2\theta$ (left) and its Fourier transform with a cut-off value of 4° $2\theta$ showing the real and the imaginary part (right).*

The main application of the exponential aberration function is to describe the peak asymmetry caused by the transparency effect, where a low absorbing sample is filled in a deep cavity of a flat plate sample holder in Bragg-Brentano geometry. The diffracted peak thus is a convolution from multi-diffraction at different depths with increasing absorption.

The cut-off value $\varepsilon_m$ as a measure for the peak asymmetry is calculated for a linear absorption coefficient $a$ in cm$^{-1}$ (Fig. 22) as

$$\delta(2\theta) = \frac{900\ \ln 0.001 \sin 2\theta}{\pi\ a\ Rs}. \qquad (70)$$

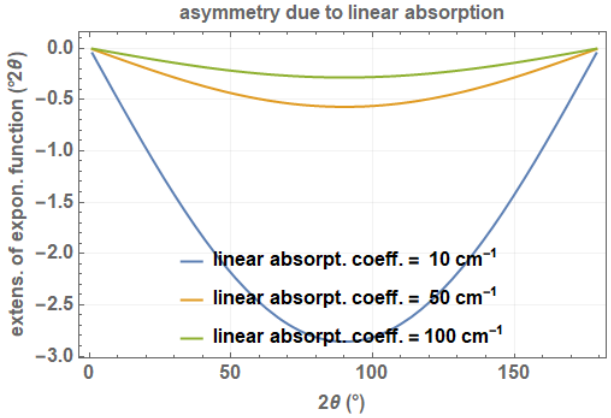

*Fig. 22: Angular dependence of the exponential function for modelling the peak asymmetry due to absorption for different absorption coefficients of 10, 50, and 100 $cm^{-1}$. The secondary diffractometer radius is set to of 217.5 mm.*

A screenshot of a Mathematica script where the exponential function for describing asymmetry due to transparency is convoluted into a Voigt function is shown in Fig. 23.

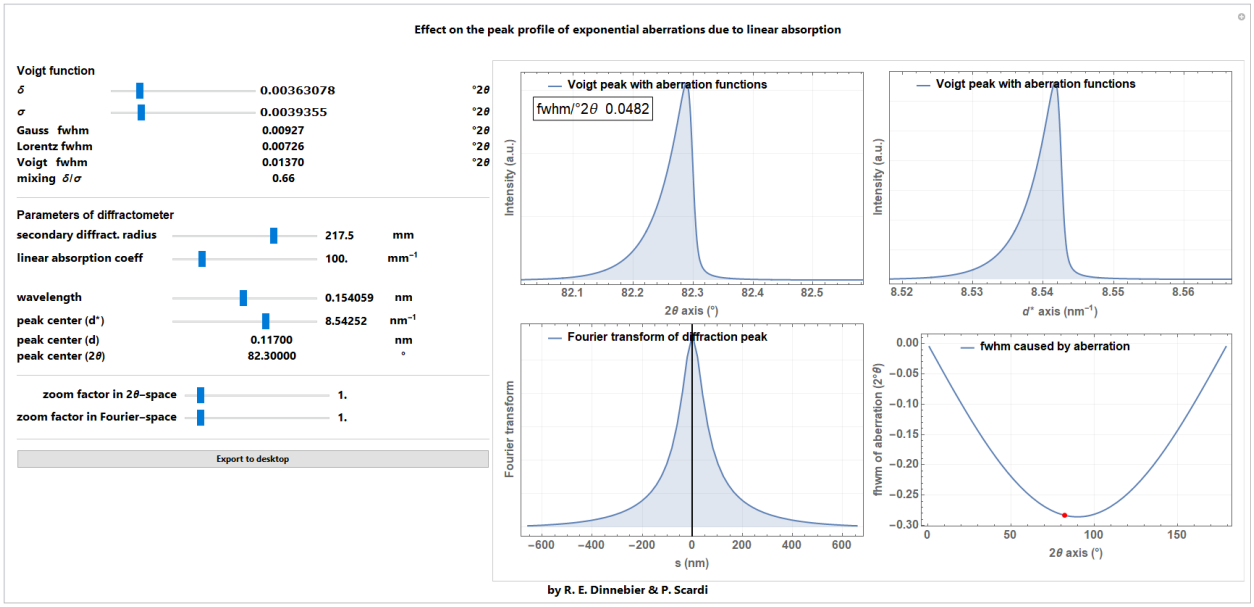


*Fig. 23: Screenshot of a Mathematica script dealing with the convolution of the exponential correction function for modelling the peak asymmetry due to the transparency effect caused by low linear absorption in flat plate samples holders with sample filled deep cavities.*

## Microstructural contribution to line profiles

Once determined, the instrumental contribution to the diffraction profile can be used constantly for a given instrument and setup. Whether it is modelled on the basis of fundamental parameters or with empirical approaches, the instrumental profile can be acquired experimentally, using appropriate powder standards (Cline *et al.*, 2013). Separately, the microstructural contribution varies for each case study, and therefore, there cannot be a universally valid model. This explains the practical use, described before, of empirical profile functions with adaptive parameters, justified by the fact that they "work well", i.e., they fit the patterns in most cases. However, the interpretation of these parameters can be misleading due to the substantial arbitrariness in the choice of profile functions and their combination (Scardi *et al.*, 2004; Scardi, 2020).

The WPPM provides a description of the microstructural component of the profile based on a convolution of terms referring to physical parameters. The two normally prevailing effects – size and

strain broadening – are introduced below, whereas other effects and more extensive discussions are reported in the literature (Scardi *et al*. 2018, Scardi, 2020, and references therein). This choice corresponds to writing Eq. 6 as

$$MS(d^*, hkl) = Size(hkl) \circ Strain(d^*, hkl)\,, \qquad (71)$$

where the Size is expressed as a function of lattice direction and Strain as a function of both lattice direction and *d**. This highlights an important property: when the diffraction profile is represented in reciprocal space, the Size component, unlike the Strain component, is independent of *d**, which allows for separation of the two effects, e.g., through the classic Warren & Averbach method (Warren & Averbach, 1950; Warren, 1990). Both components, however, can bear a dependence on Miller indices (*hkl*), respectively for the shape of the crystalline domains, and for the anisotropy of defect strain field and of the elastic medium. It is worth noting that for small nanoparticles/domains, the separation of domain size and strain parameters becomes increasingly difficult, and becomes ill-defined for very small or highly disordered domains in a crystallographic sense.

Within the limits of the so-called Tangent Plane Approximation (TPA) (Laue, 1926; Beyerlein *et al.*, 2011), it can be shown that the Fourier transform of the profile component of the Size effect, $A^S(s)$, has a simple geometric interpretation (Wilson, 1962) (Fig. 24). In fact, it corresponds to the volume of intersection *V*(*s*,*hkl*), between the crystalline domain and the same domain translated by a distance *s* along [hkl], normalized to the domain volume, $V_0$.

$$A^S(s, hkl) = V(s, hkl)/V_0 \qquad (72)$$

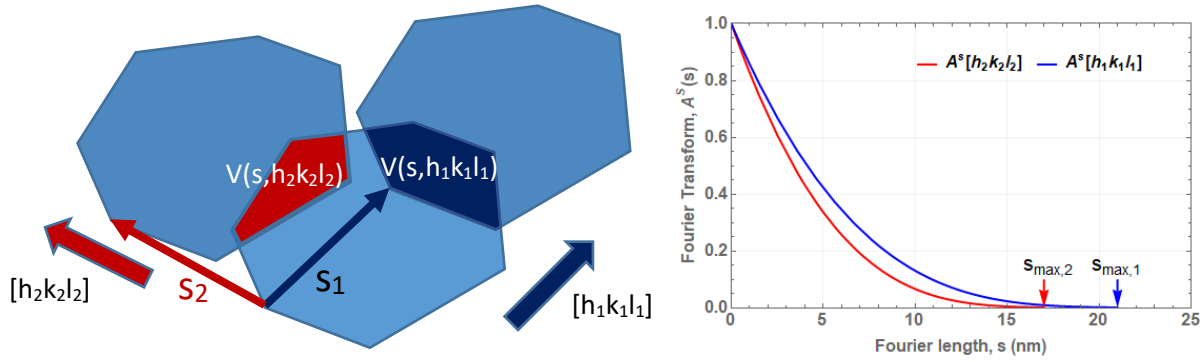


*Fig. 24: Geometrical interpretation of the Fourier transform of the Size-effect profile component. Common volume function, V(s,hkl), along two different directions, $[h_1k_1l_1]$ and $[h_2k_2l_2]$ (left) with corresponding Fourier transforms (right); $s_{max}$ stands for the maximum dimension in the crystalline domain along the given direction.*

Simple geometrical shapes allow for an easy evaluation of *V*(*s*,*hkl*) in closed analytical form (Scardi & Leoni, 2001). It is the case of frequently observed nanocrystal shapes, viz., cube, tetrahedron, octahedron, and sphere. The latter is frequently assumed even if only approximately valid, when

nanocrystals do not have a specific shape but are reasonably equiaxed. Then the Fourier transform of the line profile given by spherical domains of diameter *D* is (Fig. 25 left, red curve):

$$A^S(s) = 1 - \frac{3}{2}\frac{s}{D} + \frac{1}{2}\left(\frac{s}{D}\right)^3 \qquad (73)$$

Apart from the spherical shape, $A^S$ is generally a function of *hkl*, a dependence requiring the choice of lattice orientation within the crystalline domain. Even if complex shapes and low symmetry structures require numerical calculation methods, the calculation of $A^S$ can lead back to tractable geometry problem (Leonardi *et al.*, 2012) (Fig. 25 right).

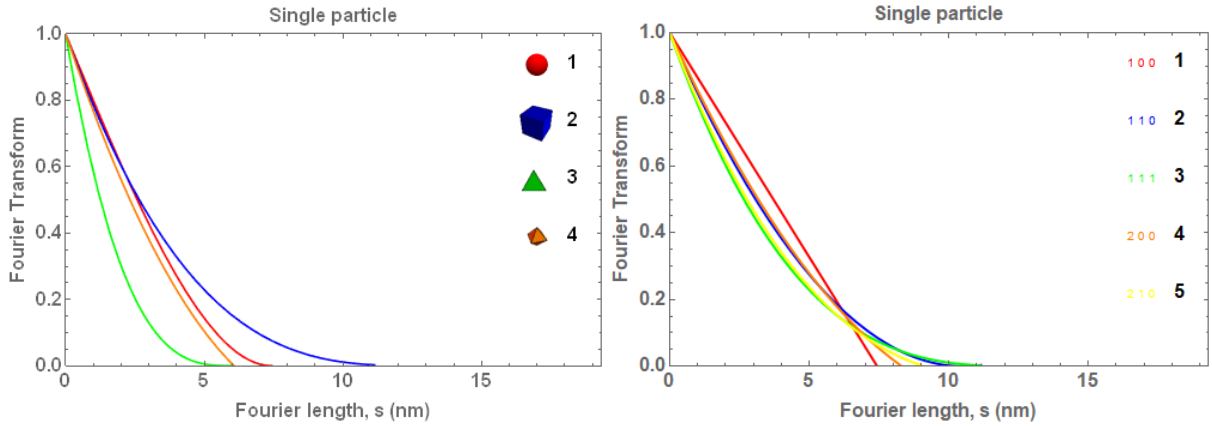


*Fig. 25: Fourier transform of the line profile given by spherical (1), cubic (2), tetrahedral (3), and octahedral (3) shaped particles in [111] direction (left) and by cubic shaped particles for different [hkl] (right): (7.4 nm diameter for sphere, and edge for cube, tetrahedron, and octahedron).*

It is unlikely that the domains, despite having the same shape, are of the same size. The problem can be addressed by considering a size distribution, as discussed in (Scardi & Leoni, 2001). A variety of distribution functions can be employed, but a lognormal distribution is often an appropriate choice (Fig. 26),

$$g_l(D) = \frac{e^{-\frac{(\ln D - \mu)^2}{2\sigma^2}}}{\sigma D\sqrt{2\pi}}, \qquad (74)$$

where lognormal mean ($\mu$) and lognormal variance ($\sigma^2$) give the central Moments, $M_{l,n}$, given by

$$M_{l,n} = e^{n\mu + \frac{n^2\sigma^2}{2}}, \qquad (75)$$

from which mean and standard deviation, respectively, are

$$M_{l,1} = < D > = e^{\mu + \frac{\sigma^2}{2}} \qquad (76)$$

$$s.d = \sqrt{M_{l,2} - M_{l,1}^2} = \sqrt{e^{2\mu+\sigma^2}\left(e^{\sigma^2} - 1\right)}\,. \qquad (77)$$

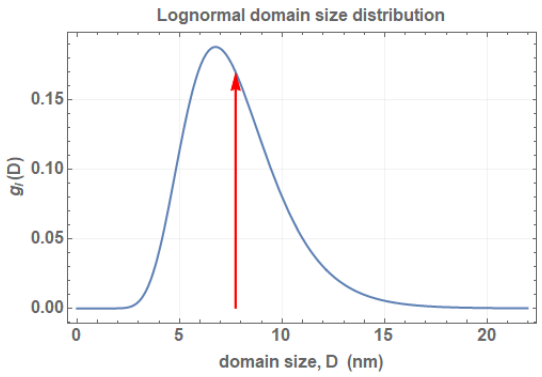


*Fig. 26: Lognormal distribution of sizes with lognormal mean $\mu$ = 1.95 and lognormal standard deviation $\sigma$ = 0.35, leading to mean size of 7.47 nm (red dart), and a standard deviation of s.d= 2.68 nm.*

It should be noted that the distribution refers to a single dimensional parameter, *D*, diameter of the sphere or edge of a cube, tetrahedron, octahedron, etc. It is theoretically possible to use more distributions, for example, base diameter and height for a cylindrical shape, but the strong correlation between the different parameters (two for each distribution) make the use impractical and refinement by least squares usually unstable.

For a lognormal distribution of spheres, the Fourier transform $A_l^S(s)$ is (Scardi *et al.*, 2018)

$$A_l^S(s) = q_0(s) - \frac{3}{2}q_1(s) + \frac{1}{2}q_3(s) \qquad (78)$$

with

$$q_n(s) = s^n \mathrm{erfc}\left[\frac{\ln s - \mu - (3-n)\sigma^2}{\sigma\sqrt{2}}\right]\frac{1}{2}\mathrm{e}^{-n[\mu+(3-n/2)\sigma^2-2\mu]}\,. \qquad (79)$$

Analogous expressions hold for different shapes, which in this case involves a direction dependence, $A_l^S(s, hkl)$:

$$A_l^S(s, hkl) = \sum_{n=0}^{3} H_n^c s^n \mathrm{erfc}\left[\frac{\ln sK^c - \mu - (3-n)\sigma^2}{\sigma\sqrt{2}}\right]\frac{M_{l,3-n}}{2M_{l,3}}\,, \qquad (80)$$

where $H_n^c$ and $K^c$ coefficients depend on the domain shape (e.g., $H_0^c$=1, $H_1^c$=-3/2, $H_2^c$=0, $H_3^c$=1/2, $K^c$=1, for spheres), and in particular $K^c(hkl)$ sets the maximum dimension in the crystalline domain along the given [hkl][6] (see Leonardi *et al.*, 2012, for other shapes) (Fig. 27).

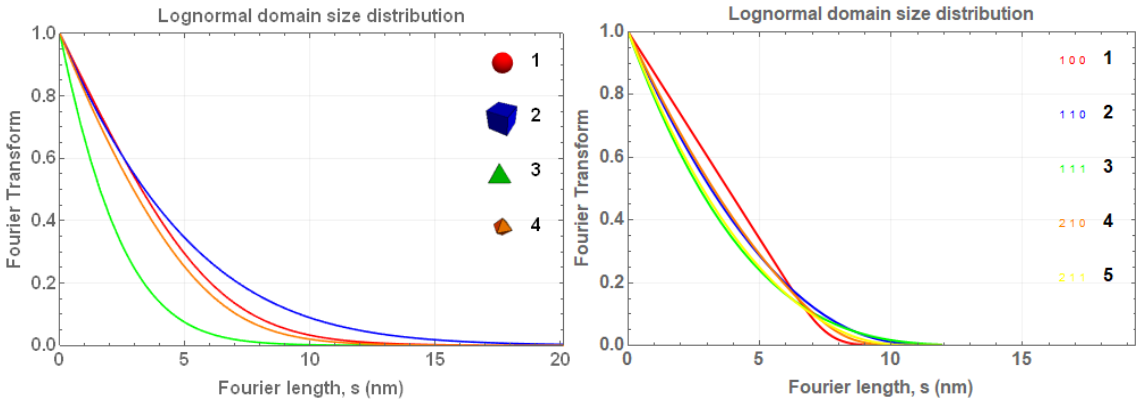


*Fig. 27: Fourier transform of the line profile of a lognormal system of spherical (1), cubic (2), tetrahedral (3), and octahedral (3) shaped particles in [111] direction (left) and by cubic shaped particles for different [hkl] (right): The parameters of Fig. 26 are used.*

The effect of a lognormal size distribution of particles with a given shape and size on the pseudo-Voigt profile and its Fourier transform is shown in Fig. 28.

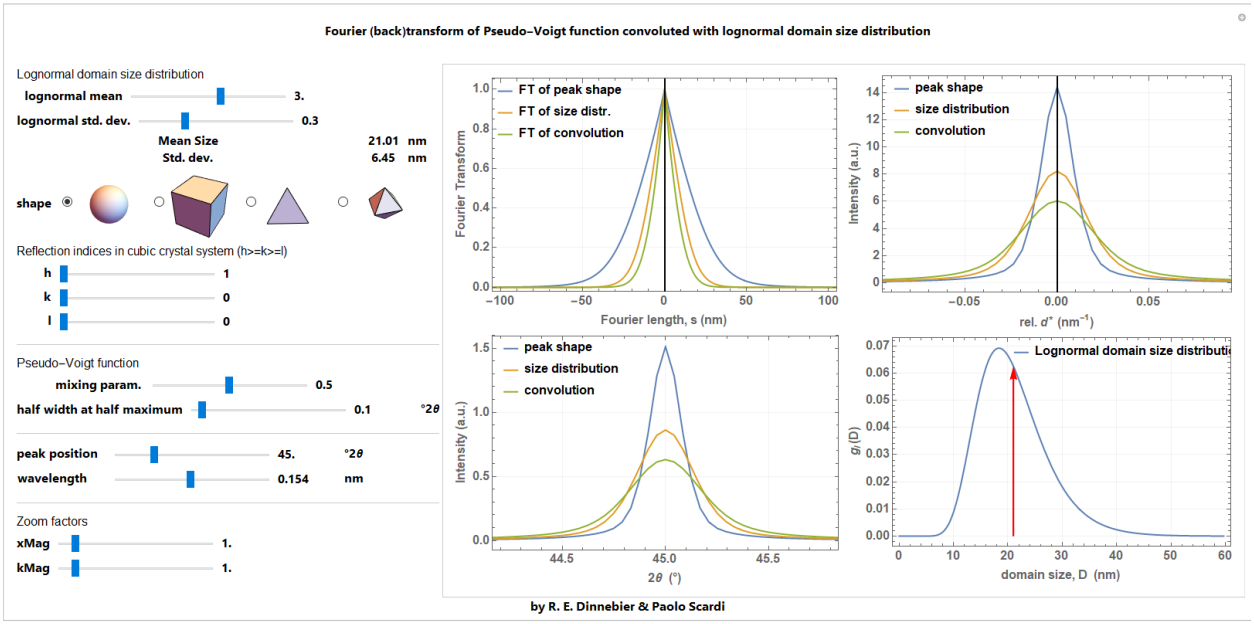


[6] The formulas for the cubic crystal system require the condition h≥k≥l.

*Fig. 28: Screenshot of a Mathematica script dealing with the convolution of size effect into a Voigt profile and its Fourier transform for a given lognormal distribution of a chosen shape*.

The WPPM approach for the Size effect is flexible enough and appropriate to deal with many real cases. It generally works if domains are not too small, because the TPA does not hold for very small sizes (≈5 nm is a realistic limit), and do not involve so-called non-crystallographic shapes like, e.g., decahedra or icosahedra, which break translational symmetry.

The Strain effect is more complex and varied than the Size effect, and can be treated in a simple way only as a perturbation of otherwise perfect crystalline domains. In these terms, it can be shown that the Fourier transform of the strain component, $A^D$, of the line profile can be approximated by (Warren & Averbach, 1952):

$$A^D(s,hkl) \cong \mathrm{e}^{-2\pi^2 d_{hkl}^{*2} < (\Delta s)_{hkl}^2 >} \qquad (81)$$

where $< (\Delta s)_{hkl}^2 >$ is the variance of the displacement distribution for any couple of scattering centres in the domain at a distance *s* along the direction [*hkl*]. This can also be written in terms of "microstrain", defined as $< \epsilon_{hkl}^2 >^{1/2} = < (\Delta s)_{hkl}^2 >^{1/2}/s$. Expressions for the microstrain can be derived for specific case studies, e.g., presence of dislocations (Wilkens, 1970a,b), or by adopting phenomenological models (Adler & Houska, 1979). In both cases, basic features are: (i) a marked dependence on the reciprocal space vector ($d_{hkl}^{*2}$ in Eq. 68); and (ii) an anisotropy specific of the elastic properties of the material and of the type of lattice defects.

If one follows the Krivoglaz-Wilkens (KW) (Wilkens, 1970a,b) approach for dislocation strain broadening, the following expression results:

$$< (\Delta s)^2 >_{hkl}^{KW} = \frac{\rho\, b^2}{4\,\pi} s^2 \Gamma_{hkl} f^*(s/R_e) \qquad (82)$$

with $\rho$ as the average dislocation density, *b* the Burgers vector modulus for the given slip system, and $R_e$ the effective outer cut-off radius of the dislocation strain field; *f** is a known (Wilkens) function of $s/R_e$ (Wilkens, 1970a), whereas $\Gamma_{hkl}$ bears the dependence on the direction, in terms of a 4th order invariant expression of the Miller indices. In the most general case (triclinic), this reads (Scardi *et al.*, 2018)

$$\begin{aligned}\Gamma_{hkl} = [&E_1 h^4 + E_2 k^4 + E_3 l^4 + 2(E_4 h^2 k^2 + E_5 k^2 l^2 + E_6 l^2 h^2) + \\ &+4(E_7 h^3 k + E_8 h^3 l + E_9 k^3 h + E_{10} k^3 l + E_{11} l^3 h + E_{12} l^3 k) + \\ &+4(E_{13} h^2 kl + E_{14} k^3 lh + E_{15} l^3 hk)]/(\, d_{hkl}^{*4} a^4),\end{aligned} \qquad (83)$$

where *a* is the first unit cell parameter according to the crystallographic conventions. Coefficients $E_1$, $E_2$, …, $E_{15}$ can be calculated for specific strain fields, like that of dislocations, given slip system and elastic constants (Martinez-Garcia *et al.*, 2009). The anisotropy factor, $\Gamma_{hkl}$, for dislocation strain is also referred to as average dislocation (or orientation) factor, $\bar{C}_{hkl}$.

Symmetry reduces the number of terms in Eq. 83 (Scardi *et al.*, 2018), down to two for the most symmetric, cubic case, for which Eq. 83 simplifies to

$$\Gamma_{hkl} = [E_1(h^4 + k^4 + l^4) + 2E_4(h^2k^2 + k^2l^2 + l^2h^2)]/(\, d_{hkl}^{*4} a^4) \\ = A + B\, \frac{(h^2k^2+k^2l^2+l^2h^2)}{(h^2+k^2+l^2)^2}. \qquad (84)$$

Values of $A$ (=$E_1$) and $B$ (=2($E_2$ - $E_1$)) can be calculated (Martinez-Garcia *et al.*, 2009) but are also known in parametric form for a wide range of anisotropy (Zener) ratios and dislocation types in cubic systems (Ungar *et al.*, 1999; Dragomir & Ungar, 2002).

As already pointed out, it is also possible to use empirical expressions, such as that named after Popa-Adler-Houska (PAH), which extends the Adler & Houska (1979) approach by including the term of anisotropy introduced by Popa (Popa, 1998; Scardi *et al.*, 2015):

$$< (\Delta s)^2 >_{hkl}^{PAH} = \Gamma_{hkl}(\alpha\, s + \beta\, s^2) \qquad (85)$$

Formally, the anisotropy factor is the same as in Eqs. 82 and 83, but in this case coefficients $E_1$, $E_2$, …, $E_{15}$ become just fitting parameters, to be optimized together with $\alpha$ and $\beta$.

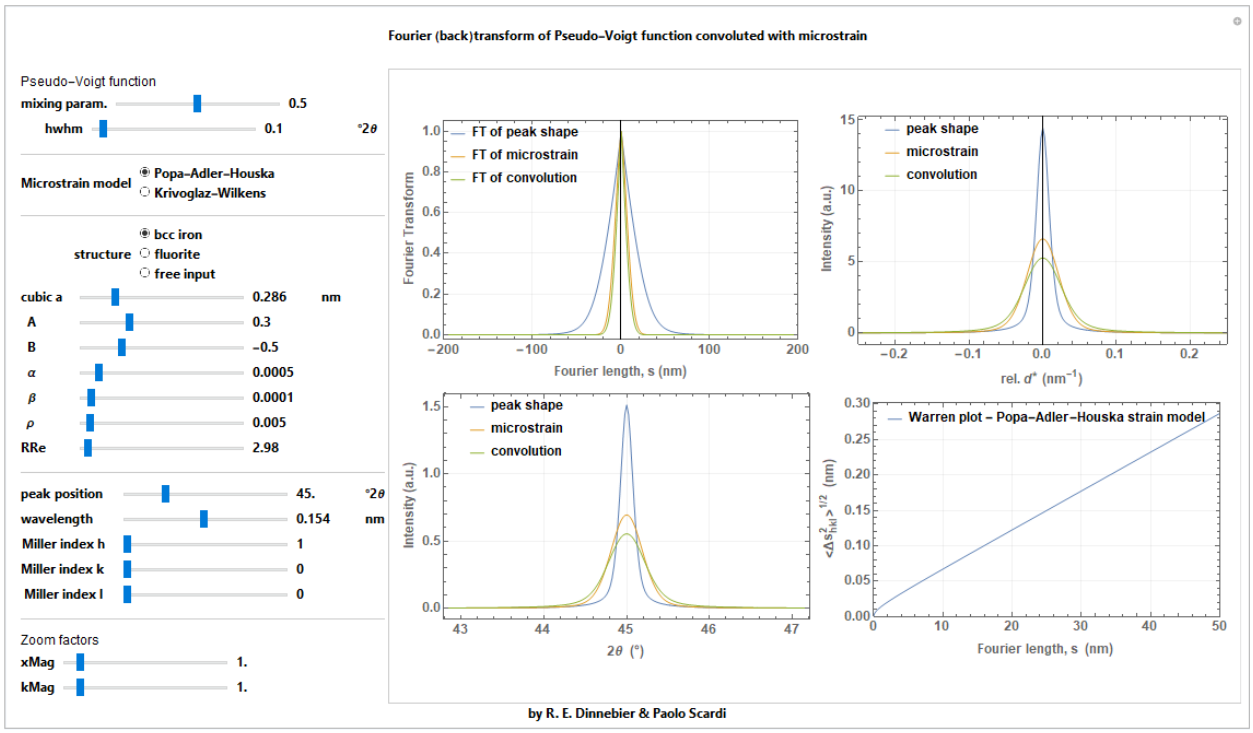


*Fig. 29: Fourier transform of the strain effect component of the line profile (top left), considering KW and PAH models, for the cases of ferritic iron (shown here) and of fluorite. Also shown are the corresponding line profiles, in reciprocal space (top right) and in 2$\theta$ space (bottom left), and Warren plot. See text for details*

Fig. 29 shows examples of applications of both models for two typical case studies, nanocrystalline bcc (body-centred-cubic) iron and fcc (face-centred-cubic) fluorite, respectively. It is interesting to note in these two examples, beyond the use of the two different models of Eq. 82 and 85, the opposite trend of the anisotropy factor. B in Eq. 84 is negative for bcc iron (like most metals) and positive for fluorite (like many binary salts), which means that stiff/soft directions are opposite: [hhh]/[h00] for iron and [h00]/[hhh] for fluorite. As a consequence, (hhh) line profiles in iron tend to less broadened than the (h00) profiles, apart from the $d^*_{hkl}$ dependence, and vice versa for fluorite. Strain broadening anisotropy definitely helps the separation of Size and Strain effects.
Microstructural effects can be visualized by two common representations, the Williamson-Hall plot (Williamson & Hall, 1953) and the Warren plot (Warren & Averbach, 1950). The former, consisting of a plot of the Integral Breadth (IB=peak area/peak max intensity) versus $d^*_{hkl}$ for as many peak profiles as are available in the experimental pattern, is also used for a preliminary assessment of the Size and Strain parameters. It is however worth noting here that this analysis (aka Williamson-Hall method) is affected by the arbitrary choice of additivity for the Size and Strain integral breadths (Scardi *et al.*, 2004). Based on the WPPM approach, instead, we can calculate the IBs from the Fourier transforms, for individual profile components and their convolution:

$$\beta_{hkl}(d^*_{hkl}) = \left[\int A(s)ds\right]^{-1} = \left[\int A^S(s,hkl)A^D(s,hkl)\ldots ds\right]^{-1} \qquad (86)$$

where the ellipsis indicates that other terms contributing to the profile can be added (e.g., the instrumental profile). The dependence on *hkl* is invariably present in the Strain term, whereas it is absent in the Size effect for the frequent case where a spherical domain shape (average) is adopted. IBs of individual profile components are also easily obtained (in analytical form in some cases) as

$$\beta^S_{hkl} = \left[\int A^S(s,hkl)ds\right]^{-1} \qquad (87)$$

$$\beta^D_{hkl}(d^*_{hkl}) = \left[\int A^D(s,hkl)ds\right]^{-1}. \qquad (88)$$

Analogous expressions hold for other possible profile components. All integrations virtually extend from -∞ to +∞, but more realistically within a finite range, determined by the maximum length for a given domain shape, and the dispersion of the size distribution. Fig. 30 shows examples of the Williamson-Hall plot where the different dependence on $d^*_{hkl}$ and on *hkl* can be seen. The different trend, with the constant size term, and the characteristic anisotropy of the Strain term, further demonstrate the possibility of separating the different effects.

The Warren plot concerns only the Strain component of the profile, and provides a convenient visualization of the dependence on s, the Fourier variable (a physical length in the crystalline domain), and anisotropy. It is a plot of $\sqrt{< (\Delta s)^2 >_{hkl}}$, the standard deviation of the displacement distribution, as a function of *s*, for different directions [hkl]. Examples are shown in Fig. 30.

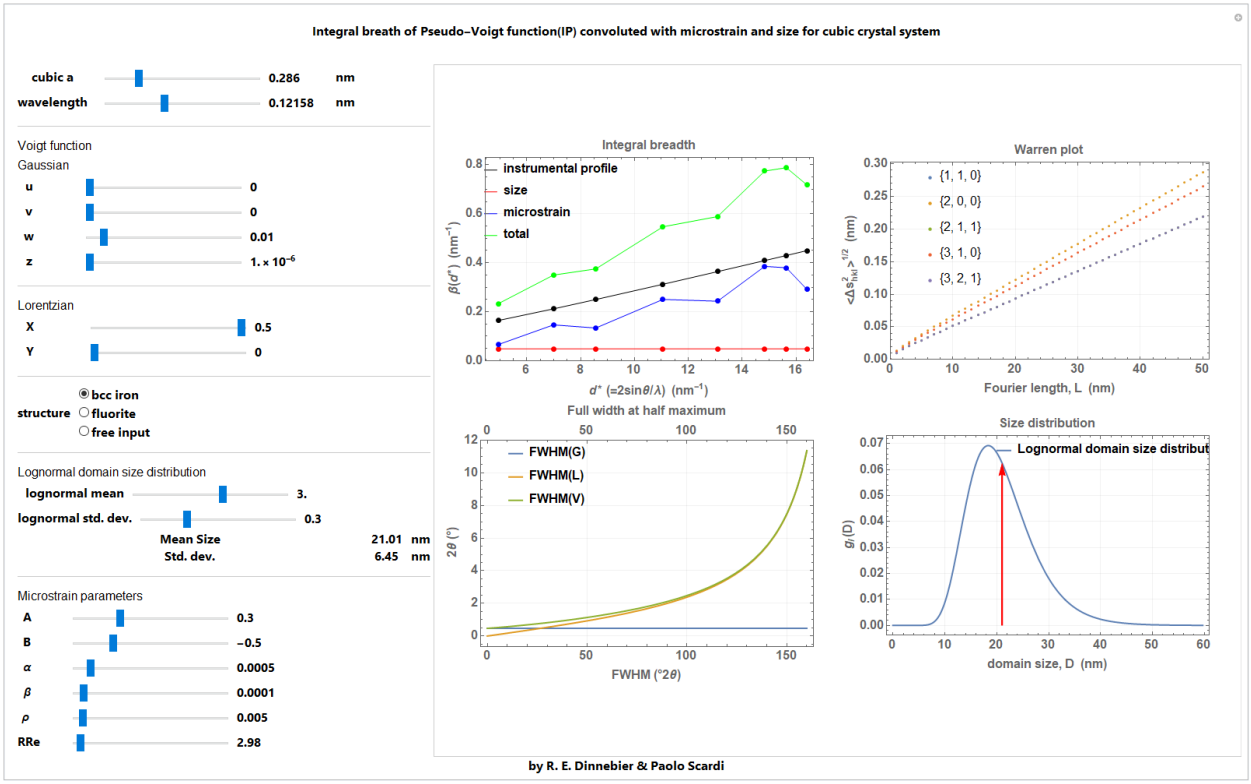


*Fig. 30: Integral breadth plot (aka Williamson-Hall plot) for the case of Figure 29 (left), considering contributions from instrument, domain size/shape and microstrain; corresponding Warren plot for some representative crystallographic directions (right).*

## Acknowledgement

We are grateful to Stefano Siboni for his help in verifying the analytical Fourier transforms of the aberration functions.

## References

Abrarov, S. M., Quine, B. M., Jagpal, R. K. (2012): *Efficient application of the Chiarella and Reichel series approximation of the complex error function,* August 10, 2012, arXiv:1208.2062 [math.GM]

Adler, T. & Houska, C. R. (1979): *Simplifications in the x-ray line-shapes analysis*. J. Appl. Phys. 50, 3282–3287.

Balzar, D. (1999): *Voigt-function model in diffraction line-broadening analysis* in Defect and Microstructure Analysis from Diffraction, edited by R. L. Snyder, H. J. Bunge, International Union of Crystallography Monographs on Crystallography.

Bergmann J., Kleeberg R., Haase A. & Breidenstein B. (2000). *Mat Sci Forum* **303**, 347–349.

Beyerlein, K.R. Snyder, R.L., Scardi, P. (2011): *Powder diffraction line profiles from the size and shape of nanocrystallites*. J. Appl. Cryst. 44, 945–953.

Bragg, W. H., Bragg, W. L. (1913): *"The Reflexion of X-rays by Crystals".* Proc. R. Soc. Lond. A. 88 (605), 428–38.

Cheary, R.W., Coelho, A.A (1992): *A fundamental parameters approach to x-ray line-profile fitting*. J. Appl.Cryst., 25 (2), 109-121.

Cheary, R.W., Coelho, A.A. (1998): *Axial divergence in a conventional X-ray powder diffractometer. I. theoretical foundations*, J. Appl. Cryst. 31, 851-861.

Cheary, R.W., Coelho, A.A., Cline, J.P. (2004): *Fundamental Parameters Line Profile Fitting in Laboratory Diffractometers*, J. Res. Natl. Inst. Stand. Technol. 109, 1-25.

Cline, J.P., Black, D., Windover, D., Henins, A. (2012): *The Calibration of Laboratory X-Ray Diffraction Equipment Using NIST Standard Reference Materials*, in Modern Diffraction Methods, edited by E. J. Mittemeijer, U. Welzel. Chapter 13, Weinheim, Wiley.

Coelho, C.C. (2018): *TOPAS and TOPAS-Academic: an optimization program integrating computer algebra and crystallographic objects written in C++*, J. Appl. Cryst. 51(1), 210-218.

Chiarella, C., Reichel, A. (1968): Journal: Math. Comp. 22 , 137-143.

Cline, J.P., Mendenhall, M. H., Black, D., Windover, D., Henins, A. (2015): *The optics and alignment of the divergent beam laboratory X-ray powder diffractometer and its calibration using NIST standard reference materials*. J. Res. NIST 120, 173-222.

Dinnebier, R.E., Billinge, S.J.L. (eds.) (2008): *Powder diffraction: theory and practice*. RSC publication ISBN: 978-0-85404-231-9, 574 pages.

Dinnebier, R.E., Leineweber, A., Evans, J.S.O. (2018): *Rietveld Refinement: Practical Powder Diffraction Pattern Analysis using TOPAS.* Berlin/Boston, *De Gruyter.*

Dragomir, I.C., Ungar, T. (2002): *The dislocations contrast factors of cubic crystals in the Zener constant range between zero and unity*. Powder Diffraction 17, 104-111.

Evans, J.S.O. (2021): https://community.dur.ac.uk/john.evans/topas_workshop/size_strain.htm

Finger, L.W., Cox, D.E., Jephcoat, A.P. (1994): *A correction for powder diffraction peak asymmetry due to axial divergence* . J. Appl. Cryst. 27, 892-900.

Klug, H.P, Alexander, L.E. (1974): *X-ray diffraction procedures for polycrystalline and amorphous materials*, John Wiley and Sons, New York, USA, 992 pages.

Laue, M. von (1926): *Lorentz-Faktor und Intensitätsverteilung in Debye-Scherrer Ringen*. Z. Kristallogr. 64, 115–142.

Leonardi, A. Leoni, M., Siboni, S., & Scardi, P. (2012): *Common volume functions and diffraction line profiles of polyhedral domains*. J. Appl. Cryst. 45, 1162–1172.

Martinez-Garcia, J., Leoni, M. & Scardi, P. (2009): *A general approach for determining the diffraction contrast factor of straight-line dislocations*. Acta Cryst. A65, 109–119.

mathematica stackexchange question 19884:
https://mathematica.stackexchange.com/questions/19884/compiling-the-voigtdistribution-pdf

mathematica stackexchange question 1714:
https://mathematica.stackexchange.com/questions/1714/numerical-fourier-transform-of-a-complicated-function/151179#151179

mathematica stackexchange question 19905:
https://mathematica.stackexchange.com/questions/19884/compiling-the-voigtdistribution-pdf/19905#19905

Mendenhall, M.H., Henins, A., Hudson, L.T., Szabo, C.I., Windover, D., Cline, J.P. (2017): *High-precision measurement of the X-ray Cu Kα spectrum*. J Phys. B Mol. Opt. Phys. 50, 115004 18pp.

Olivero, J. J.; R. L. Longbothum (1977): *Empirical fits to the Voigt line width: A brief review.* Journal of Quantitative Spectroscopy and Radiative Transfer. ***17*** *(2): 233–236.*

Popa, N. C. (1998): *The (hkl) Dependence of Diffraction-Line Broadening Caused by Strain and Size for all Laue Groups in Rietveld Refinement*. J. Appl. Cryst. 31, 176–180.

Press, W. H., Teukolsky, S., Vetterling, W. T., Flannery, B. P. (2007): Numerical recipes: The art of scientific computing, Publisher: Cambridge University Press, UK, 3rd edition, 1256 pages.

Scardi, P., (2020): *Diffraction line profiles in the Rietveld method.* Cryst. Growth Des. 20, 6903-6916.

Scardi, P., Azanza Ricardo, C. L., Perez-Demydenko, C., Coelho, A. A., (2018): *Whole powder pattern modelling macros for TOPAS*. J. Appl. Cryst. 51, 1752−1765.

Scardi, P., Leonardi, A., Gelisio, L., Suchomel, M. R., Sneed, B. T., Sheehan, M. K. & Tsung, C. K. (2015): *Anisotropic atom displacement in Pd nanocubes resolved by molecular dynamics simulations supported by x-ray diffraction imaging*. Phys. Rev. B, 91, 155414.

Scardi, P., Leoni, M. (2001): *Diffraction line profiles from polydisperse crystalline systems.* Acta Cryst. A 57, 604-613.

Scardi, P., Leoni, M. (2002): *Whole powder pattern modelling.* Acta Cryst. A 58, 190-200.

Scardi, P., Leoni, M., Delhez, R. (2004): *Line broadening analysis using integral breadth methods: a critical review*. J. Appl. Crystallogr. 37, 381–390.

Scherrer, P. (1918): *Bestimmung der Größe und der inneren Struktur von Kolloidteilchen mittels Röntgenstrahlen*. In: *Nachrichten von der Gesellschaft der Wissenschaften zu Göttingen, Mathematisch-Physikalische Klasse*. Weidmannsche Buchhandlung, Berlin, S. 98–100

Schoening, F. R. L. (1965): *Strain and particle size values from X-ray line breadths*. Acta Cryst. (1965). 18, 975-976.

Thompson, P., Cox, D. E., Hastings, J. B. (1987): *Rietveld refinement of Debye-Scherrer synchrotron X-ray data from $Al_2O_3$*, J. Appl. Cryst. 20, 79-83.

Ungar, T., Dragomir, I., Revesz, A. & Borbely, A. (1999): *The contrast factors of dislocations in cubic crystals: the dislocation model of strain anisotropy in practice*. J. Appl. Cryst. 32, 992–1002.

Van Laar & Yelon, J. (1984): *The peak in neutron powder diffraction*. J. Appl. Cryst., 17, 47-54.

Voigt, W. (1912): *Das Gesetz der Intensitätsverteilung innerhalb der Linien eines Gasspektrums*. Sitzungsbericht der Bayerischen Akademie der Wissenschaften, Band 25, 603–620.

Von Dreele R.B. (2008): *Rietveld Refinement* in Powder diffraction: theory and practice, (eds. R.E. Dinnebier and S.L.J. Billinge), RSC Publishing, Cambridge, pp. 266- 281.

Young, R.A. (1993): *Introduction to the Rietveld method*. - The Rietveld Method, edited by R.A. Young, IUCr Book Series, Oxford University Press, UK, 1-39.

Warren, B.E. (1990): *X-Ray Diffraction*. New York, Dover Publications Inc.

Warren, B.E. & Averbach, B.L. (1950): *The Effect of Cold-Work Distortion on X-Ray Patterns*. J. Appl. Phys. 21, 595–599.

Warren, B.E. & Averbach, B.L. (1952): *The Separation of Cold-Work Distortion and Particle Size Broadening in X-Ray Patterns*. J. Appl. Phys. 23, 497.

Weisstein, Eric W. (2021): "*Convolution*" From MathWorld--A Wolfram Web Resource: https://mathworld.wolfram.com/Convolution.html

Wilkens, M. (1970a): *The Determination of Density and Distribution of Dislocations in Deformed Single Crystals from Broadened X-Ray Diffraction Profiles*. Phys. Status Solidi A, 2, 359-370.

Wilkens, M. (1970b): *Theoretical aspects of kinematical X-ray diffraction profiles from crystals containing dislocation distributions*, in Fundamental Aspects of Dislocation Theory, National Bureau of Standards (US) Special Publication No. 317, Vol. II, edited by J. A. Simmons, R. de Wit & R. Bullough, pp. 1195-1221. Washington, DC: National Bureau of Standards

Williamson, G. K. & Hall, W. H. (1953): *X-ray line broadening from filed aluminium and wolfram*. Acta Metall. 1, 22-31.

Wilson, A.J.C. (1962): X-ray Optics: The Diffraction of X-rays by Finite and Imperfect Crystals. London: Methuen and Co.

Wolfram Research, Inc., Mathematica, Version 12.2, Champaign, IL (2020).